NEUROTECHNOLOGY DESIGN FEATURES' IMPACT ON THE FUNCTION AND IDENTITY OF REACTIVE ASTROCYTES

By

Ti'Air Riggins

A DISSERTATION

Submitted to
Michigan State University
in partial fulfillment of the requirements
for the degree of

Biomedical Engineering – Doctor of Philosophy

2021

ABSTRACT

NEUROTECHNOLOGY DESIGN FEATURES' IMPACT ON THE FUNCTION AND IDENTITY OF REACTIVE ASTROCYTES

By

Ti'Air Riggins

Implantable neurotechnology offers substantial promise to improve the condition of many neurodegenerative diseases. Microelectrode arrays implanted in the brain have the capability to stimulate or record electrical activity from neighboring cells. However, shortly after implantation, a foreign body response occurs, which is what researchers believe decreases the electrical recording stability and longevity of signal detection of these devices. Established biomarkers such as astrogliosis, and stimuli such as the mechanical mismatch at the device-tissue interface, have been studied to understand the tissue response to the devices. However, the relationship of these factors with device performance is not well understood. Astrocytes play an important role in the brain's immune system and recently, RNA analysis has confirmed transcriptional profiles of reactive astrocytes which are associated with specific injury states and neurodegenerative diseases. In this dissertation, I have investigated new biomarkers of astroglial reactivity at the electrode interface and characterized the surface topography and bending stiffness of devices. I induced two types of inflammatory astrocytic cell culture models, and I characterize each model's reactivity in comparison to gene expression surrounding electrodes implanted in rat tissue. Atomic microscope microscopy (AFM) techniques were also used to measure surface roughness and bending stiffness as it may predict cellular adhesion and device performance. I aim to elucidate pathways in the neurological foreign body response which will give researchers new potential biomarkers to target to improve recording performance, motivating improved designs for implantable neurotechnology.

The research presented in this dissertation investigates how design features influence the tissue interface and asks questions about possible ways to mitigate tissue response: (1) by exploring and summarizing the design space as a whole, suggesting ways to characterize designs and evaluating each designs' successes and limitations (2) using a cutting edge imaging technique to image and

measure material properties of three commonly used materials, (3) and creating a reactive tissue culture model, comparing its proteomic and genetic expression to the established rat model. Chapter 2 describes surface characterization techniques that could be used to better classify device features to predict performance and explores next generation probes from a design and performance standpoint. Chapter 3 uses atomic force microscopy to image and measure surface roughness on device surfaces while also measuring the bending stiffness to help determine possible micromotion in the brain. Here, we speculate what these findings mean for the performance and longevity of current probe design. Chapter 4 develops an astroglial culture model to mimic foreign body response in the brain and compare the genomic results to tissue culture near and far from the implanted device. Here, we report the transcriptomic results of the model in comparison to brain transcriptomic results, and what these biomarkers may implicate regarding tissue response and neurodegenerative signaling.

This body of work uncovers knowledge recapitulating important factors of device features that affects tissue signaling at the tissue device interface, and biomarkers that play a role and cell signaling. Future directions aim at developing a more physiologically relevant tissue culture model that can predict clinical outcomes, and use high throughput screening techniques to help researchers address the challenge of long term suboptimal device performance.

To all of the Black girls who have ever been pushed out or told they do not belong in STEM.

ACKNOWLEDGEMENTS

Two pages really isn't enough space for thanking my village for literally yeeting me over the finish line to get here. First, I would like to thank my adviser, Erin Purcell for taking a chance on me and giving me the time to interview after hearing about my situation and longing to stay in neural engineering to finish. You are literally the only PhD adviser I have ever had that have taken the time out to teach me lab techniques one on one, allowed me to take ownership of my work, mentored me and believed in me. Without you, I never would have made it here. Thank you for the opportunity of showing me what effective mentorship looks like.

I'd like to thank my extended family of mentors – Theo Nicholson, Marguerite Matthews, Edwin Lee and Adrienne Madison who have been there for and with me every step of the way, whether I was complaining about something, trying to make sense of everything that was happening or just getting through the day. Thank you for empowering me to understand that my first PhD advisers and institution do not get to dictate my narrative. I also would like to thank my SfN #NSPeeps, DSPAN & Black In Neuro family for the opportunity to be mentored, and guided by some of neuroscience's best scholars and people who cared about my trajectory. The amount of opportunity and support is immeasurable. I would also like to think my family and friends who stuck by my side and encouraged my every move and decision. Thanks for stopping to ask me when I was going to be done years ago (lol). Thanks for confiding in me with unfortunate shared and lived experiences. Thank you for letting me know that my trauma does not define me, I am loved, and I am greater than my struggles.

Thank you to my committee and project mentors who help bring this research to life. Thank you, Steve and Marie Claude, for your patience in explaining ideas, rationale and training me hands on technique. Thank you, Kris, Masako, Tk and Wen, for your input and guidance. Thank you all for bringing me into your scientific family and guiding me down the right path, treating me as a colleague capable of doing research. This is my first time having a supportive training environment and I will take bits and pieces of each mentorship style with me as one day, I will manage my own

lab. Special thank you to Dr. Kathy Walsh who took a whole week out of her schedule to further train me on the AFM and troubleshoot and figure out solutions to imaging these very tiny probes.

I'd like to thank my lab members who took time out of their day to show me how to perform lab technique without making me feel bad about but also explaining things to me as if I was capable – Thank you Monica, Bailey and Cort. Also not a thank you but our undergrads are rock stars and I look forward to the work Kathleen, Emani and Nick do in the future. Also, thank you to the rest of the lab for your presence and kindness.

Also, thank you Dana and Katy for recruiting me here and hearing my side of the story. Thank you for all the faculty I met with after attending ComSci Con MI for the first time in 2018, just days after my ambush of a prelim. Thank you for believing me and encouraging me to stay in grad school. Also thank you to my ComSci Con MI crew for help facilitating these much needed connects, in particularly Jessica and Chelsie who were making connections for me to get out of Indiana.

. . . the motivation for me is them telling me what I could not be. Oh well.

TABLE OF CONTENTS

LIST OF TABLES

LIST OF FIGURES

CHAPTER 1

INTRODUCTION

1.1 The Potential of Implantable Neurotechnology: A Developmental Timeline

1.1.1 Introduction and Applications

A stroke caused a woman to become a tetraplegic, losing the function of her extremities and having to depend on others. In 2005, she was chosen to be a part of pilot clinical studies, now famously known as the BrainGate trials. After a craniotomy, in which microelectrode arrays (MEAs) were implanted into her motor cortex, the patient endured a month of training in which neural activity patterns were collected and mapped out. The recorded activity was decoded into algorithms that translated to movement for a robotic arm. For the first time in over a decade, the patient was able to gain some level of independence, using her mind to communicate with a robotic arm, and allowing her to drink from a cup (Ajiboye et al. (2017); Hochberg et al. (2006); Simeral (2011); Kim et al. (2008); Hochberg et al. (2012); Simeral (2011)). This technology has tremendous potential to also treat multiple sclerosis, epilepsy, Alzheimer's, Parkinson's disease and offer an alternative to chronic pain management. However, a major roadblock in this area of research presents itself as the instability and limited longevity of recorded signals elicited from neurons, detected by implantable neurotechnology. For decades, researchers have noticed the eventual loss and signal is accompanied with neuronal death in a common area around the implantation site of probes, known as the "kill zone", which is roughly 200μm within probe insertion site (Biran et al. (2005); Edell et al. (1992)). As result, researchers suspect that foreign body response (FBR) is the culprit for inevitable loss in probe function. A better understanding of this complex biological response offers a more intimate knowledge base of the relationship between glial signaling pathways in response to neurotechnology design features that lead to loss in electrode performance over time.

1.1.2 History and Milestones of Neurotech Development

The first set of implantable electrodes capable of chronic recording were developed in the 1950s. These tungsten insulated microwires were used to detect neural activity in live animals Strumwasser (1958), which lasted for about a week. This groundbreaking study displayed constant waveforms with consistent amplitudes, demonstrating that it was possible to study the same neuron within a living organism. This seminal paper provided the fundamental science behind the recording electrodes that are used in designs today. In 1969, a second foundational paper demonstrated that conditioning and positive reinforcement could influence cortical neuron firing activity and be measured by electrodes Fetz (1969). During the 1970s, the development of photolithographic and silicon etching techniques provided new rapid prototyping fabrication methods. These first silicon-based multielectrode arrays designed by Wise, Starr, and Angel (Wise et al. (1970); Wise & Angell (1975)) became the precursor for the so-called "Michigan" Array. Given that these fabrication methods provided a costly barrier to entry in during this time, development in the field did not see a significant increase in the rate of device development until the 1990s.

Multiple recording sites patterned on each shank allowed for the Michigan array to achieve high spatial resolution while enabling interrogation of activity along the depth of the device; these were advances to the microwires of the 1950s. This "passive" silicon-based array is fabricated with a grow-and-pattern mask in which boron is diffused into the substrate, and then layered with lower dielectrics, pattern conductors and upper dielectrics. During the third step, areas for contact on the dielectric surfaces is made through bond pads and liftoff sites. The final step involves the etching of field dielectrics, in which the probe is released from the substrate (Wise et al. (2004)). "Active" Michigan arrays are considered such, because they are patterned with complementary metal oxide semiconductor (CMOS) circuitry in their design that has allowed for in vivo recordings (Bai & Wise (2001)). These designs consist of a geometric 3D probe, assembled in a 3 x 3 or 4 x 4 matrix on 200 μm centers that have an average distance of 24μm between each shank, a gain of 40dB, input resistances measured 80-500MΩ, and a bandwidth of 13kHz (Bai & Wise (2001)). This high density design equipped with on-chip pre-amplifiers decreased movement related artifacts in vivo

and could record from dendrites and soma of the same neuron (Csicsvari et al. (2003)). Polytrodes allow for improved classification of individual neurons with similar waveform characteristics, in an advance to the conceptually-similar 1970s tetrode based wire design (Blanche et al. (2004)). Lastly, Michigan arrays more recently have incorporated flexible polymers for chronic cortical recording (Hetke et al. (2003)).

A similar shank design is also used for the Utah array, the probe that is used in the Braingate trials, which is the only FDA cleared electrode for chronic recordings (Kim et al. (2008)), and also uses a wet etching batch fabrication process. The Utah array consists of 100 sharpened silicon needles coated with platinum, which allows for neural charge transfer, that uses a n-type wafer, micromachined with a gold wire (Campbell et al. (1991)). Each 0.09 mm thick, 1.5mm long needle is electrically isolated from other needles, uses thermomigration to increase silicon conductivity. There is also a slanted version of the Utah array, in which the needle shaft lengths range from 0.5 to 1.5 mm, row by row, to accommodate fibers of the cochlear nerve at multiple depths (Badi et al. (2003)). The Utah array has been used in the dorsal root ganglion, cat visual and auditory cortex (Rousche & Normann (1999)) and the parietal cortex (Suner et al. (2005)).

By the late 1980's, labs began to investigate the tissue response to implantable materials. Parylene-c was considered a promising material, as it was classified by the FDA as biologically inert. Building on promising results from parylene-c insulated microelectrodes (Bak et al. (1977), parylene-c coated probes afforded an 1000+ day chronic recording in monkeys, with a low impedance Schmidt et al. (1988)). These results ushered in a wave of other polymer-based electrodes aimed at improved tissue integration and chronic stability. Flexible polyimide-based cuffs have been used to physically support and integrate regenerated nerves (Kovacs et al. (1992)) and nerve fibers (Stieglitz et al. (1997)). Other polyimide applications have been integrated in flexible cable-like probes, which have been micromachined in 200-300 nm thick layers for acute and chronic recordings (Stieglitz (2001)). Microfluidic structures, fabricated via lamination techniques (Metz et al. (2004a, 2005)), have been developed for microdialysis and drug delivery (Metz et al. (2004b)). Besides utilizing softer substrate materials, researchers have also improved performance

by increasing contact density, as well as developing insertion approaches that allow soft arrays to stiffen initially to penetrate the dura (Chung et al. (2019)).

Many of the probe designs created in the last decade have been a conglomeration of the earlier designs, as researchers continue to improve the chronic stability and flexibility of electrode arrays. New approaches can be classified into three main areas: probes with biological coatings, probes with non-biological coatings, and probes designed for drug delivery. Unfortunately, many of these new designs are accompanied with their own limitations that contribute to probe instability, such as limited stability of coatings, biofouling, limited knowledge of material biocompatibility, and a burst effect of drug release (Thompson et al. (2020)). Common issues observed with current probe stability design will be highlighted in the following section.

1.1.3 Problems with Signal Instability, Loss, and Shifting Stimulation Thresholds

Although the impact of implantable electrodes is profound, an ongoing challenge in this field is presented by the instability and limited longevity of recorded signals detected by surrounding neurons. Recently, researchers in this field have categorized the causes of device failure in four main areas: mechanical, material, electrical and biological. Regardless of cause, device failure has been determined as loss of the ability to record and transmit action potentials on all electrode channels on an array, in which local field potential (LFP) data collection is not consistent across arrays (Barrese et al., 2013). To characterize and predict possible failure modes for clinical studies, a longitudinal study on device failure, using nonhuman primates, produced results of an overwhelming 79% (62) arrays failed, where only 9% (7), remained functional until the end of the trial 387 days post implantation. Of these failures, 73% were acute, meaning that these failures occurred less than a week post implantation (Barrese et al. (2013)). In a separate study investigating the change in recording capacity over time in rhesus macaques, a 2.4% average monthly decline in the peak-to-peak signal amplitude of the largest recorded unit occurred (Chestek et al. (2011)). A brief summary of various device failure observations amongst common probe designs, that possibly contribute to suboptimal long-term stability, follows:

1.1.3.1 Mechanical

In the study referenced above, 56% of mechanical failures were related to the skull base connector (Barrese et al. (2013)). In another study, micromotion was determined to occur from mismatch in device and brain tissue moduli, and brain pulsation, Lee et al. (2005) which indirectly causes electrophysiological recording drifts (Michelson et al. (2018)). Other areas of mechanical mismatch occur at the iridium metal-silicon substrate interface of electrodes, with highest strain measurements observed at the needle tips and other prominent geometric features located at the distal ends of the probe Kozai et al. (2015a). Cracking and delamination occurs in the highest rates in vivo at these sites (Kozai et al. (2015a)).

1.1.3.2 Material and Electrical

A progressive decrease in electrical signal amplitude over time, combined with changes in impedance, was accompanied by insulation leakage, electrode breakages, electrical coating delamination, and material cracking along the electrode shafts (Barrese et al. (2013)). This, in turn, creates potential physical barriers for neuron-to-probe communication and signal shunting (Schmidt et al. (1988)). Likewise, deeper recording sites require longer electrical traces to travel up the shank, increasing the probability of a breakage in the trace (Kozai et al. (2015a); Michelson et al. (2018)) .

1.1.3.3 Biological

Early observations of neuronal loss and glial encapsulation surrounding implanted electrodes indicated that the tissue response to devices likely plays an important role in long-term stability and longevity (Szarowski et al. (2003); Biran et al. (2005)). In a subsequent study by (Barrese et al. (2013)), 53% of chronic failures were characterized by meningeal encapsulation (Barrese et al. (2013)). Fibroblasts invaded the dura and arachnoid spaces, creating a nascent parenchymal boundary in the subdural space (Shearer & Fawcett (2001)). It has also been observed that larger interstitial space in primate brains (2-4 mm) versus the smaller spaces in rodent brain (0.1-0.2

mm) can also allow more displacement resulting in higher strain (Kozai et al. (2015a)). At the molecular level, these interstitial spaces may be damaged by probe insertion, where upregulation in proinflammatory cytokines such as Il-1β follows activation of caspase-1 (Kozai et al. (2015a)). While these observations underscore the need to explore the biological response to electrodes, several questions remain. Michelson et al. (Michelson et al. (2018)) describe several sources of complexity in interpreting device-tissue interactions, including misalignment of histology with recording quality (i.e., poor recording quality despite tissue stained with little loss of NeuN, suggesting minimal tissue damage) (Michelson et al. (2018)). Furthermore, it has been observed that neurons near the implantation site undergo structural and functional changes, as firing shifts from a hypo- to hyper-excitable state as indicated by change in sodium to potassium ion channel activity (Salatino et al. (2019)). In summary, these nuanced complexities motivate a more systematic approach to improving recording loss and device stability, from a biological standpoint.

1.2 Stereotypical Pathophysiologic Response to Implantable Neurotechnology

The stereotypical pathophysiologic response to implanted MEAs occurs in the following stages: (1) device insertion typically causes mechanical damage to tissue, breach of the blood-brain barrier (BBB) and disruption of vasculature at the implantation site; (2) microglia are activated to encapsulate the probe immediately thereafter, creating a physical barrier responsible for limiting ionic exchange with the probe while potentially releasing inflammatory cytokines; and (3) reactive astrocytes form an encapsulating sheath around the electrodes in the following weeks, increasing impedance as (4) neuronal loss ensues within the recordable radius of the injury site (Kozai et al. (2015a)). This last phase, in which astrocyte function plays a complex role in the immune response and device performance, remains poorly understood. In this section, **figure 1.1**, I will detail each stage of response.

1.2.0.1 Device insertion

Once probe insertion severs the BBB and blood vasculature, tissue displacement occurs resulting in increased tissue strain, followed by a buildup of cell and tissue debris. This initiates signaling

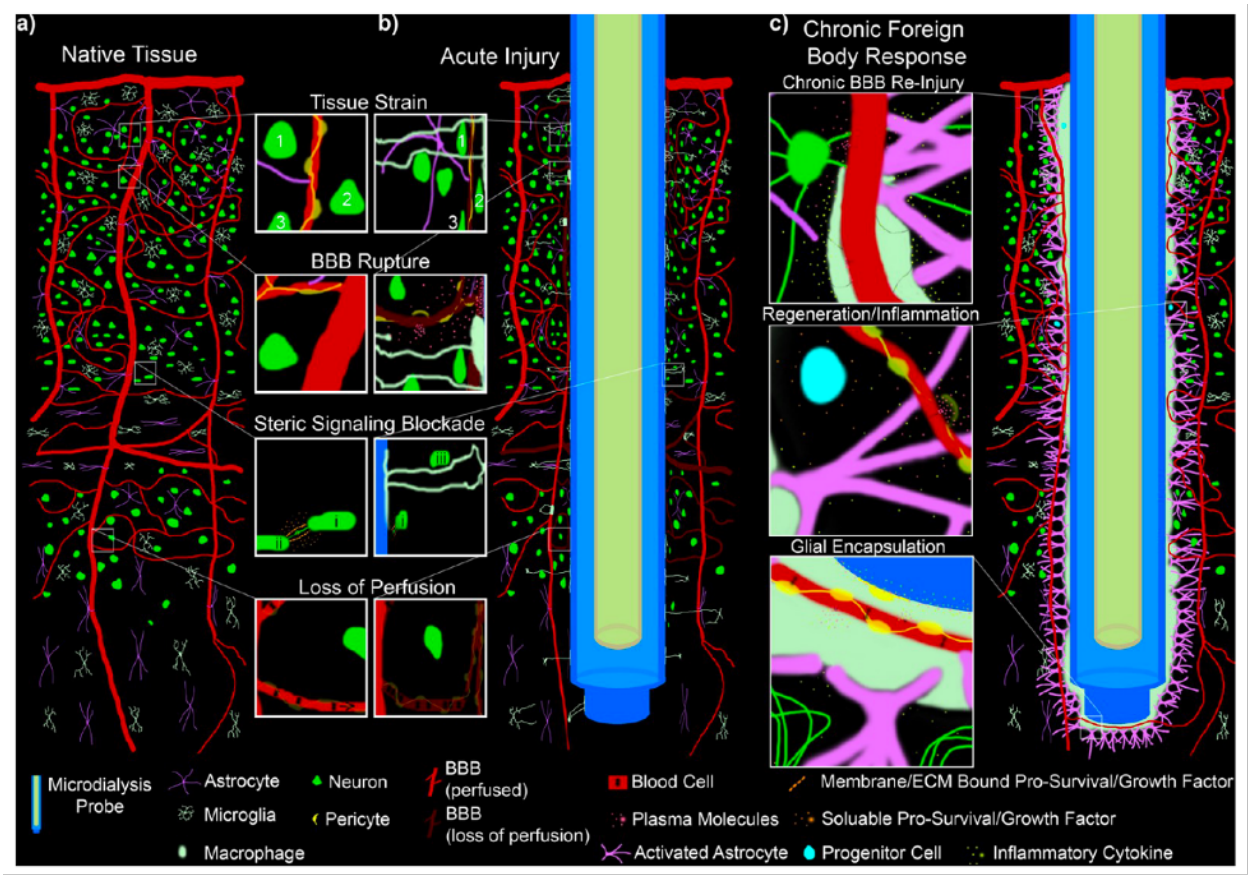

Figure 1.1: Tissue response before and after probe insertion (Kozai et al. (2015a))

cascades responsible for inflammation, which also prevents blood perfusion (Kozai et al. (2015a)). In this instance, the microenvironment buildup of blood and debris blocks efficient neurotransmission and perfusion loss occurs. During perfusion loss, damage-associated adenosine tri-phosphate (ATP) is released which triggers an ATP gradient at the astrocytic processes, which is then sensed by the P2Y purinoceptor 12 (P2RY12) of microglia (Li & Barres (2017).

1.2.0.2 Acitvated Microglial

Microglia comprise 5-10% of the cells of the central nervous system (CNS) (Li & Barres (2017)). Given that the CNS is highly vascularized and circulates myeloid cells, dendritic cells, granulocytes, classical monocytes ($Ly6C^{16}$ in mice, CD^{14} $hiCD^{16}$ in human) and non-classical patrolling monocytes ($Ly6C^{low}$ in mice, CD^{+} $hiCD^{16}$ in human) (Li & Barres (2017)) the reaction to the damage-associated ATP gradient is almost instant. During BBB breach, or certain

disease states, Ly6C^{hi} sense signaling changes within the microenvironment, infiltrate the brain parenchyma, and differentiate into microglial-like cells. In this transition, environmental cues determine which type of factors that are released; transforming growth factor β (TGFβ) modulates microglial activation and is released for anti- and pro-inflammatory conditions (Li & Barres (2017)). Under pro-inflammatory conditions, microglia become perivascular macrophages, which downregulate microglial-specific transcription factor SALL1 and upregulate genes specific to perivascular macrophages (Cd45, Cd206, and Cd74). In turn, these cells take a more active role in synapse modulation (Li & Barres (2017)). Although microglial-synapse interactions are yet to be fully understood, there is evidence that microglia are involved with synapse remodeling (Li & Barres (2017); Liddelow et al. (2017)). Microglia are the only cells in the brain that express complement component C1q (C1q) and complement receptors 3 and 5 (CR3, Cr5) (Li & Barres (2017)), which tag weak synapses and phagocytose them.

1.2.0.3 Reactive Astrocytes

Astrocytes become reactive in concert with microglia and simultaneously sense microenvironment changes through their end processes. Because there is an increase in ATP in the microenvironment, the γ subunits on G-coupled proteins become phosphorylated. This environmental change outside of the cells, sends signals to phosphorylate, ubiquitinate and send parts of the factor kappa-light-chain-enhancer of activated B cells (NF-κB) complex to a proteasome, freeing (NF-κB) (Liu et al. (2017). Untethered inside of the cell, it can migrate to the nucleus, bind to DNA, and turn on certain genes (Liu et al. (2017)). This particular activated path produces neuro-inflammation cytokine signaling. Based on the type of injury, astrocytes will either release neurotrophic factors including basic fibroblast growth factor (bFGF), vascular endothelial growth factor (VEGF), and brain-derived neurotrophic factor (BDNF) or pro-inflammatory factors including interleukin 1 beta (IL-1β) tissue necrosis factor alpha (TNF-α) and nitric oxide (NO) (Li et al. (2019)). Since C1q and C3 are only expressed in pro-inflammatory microglia and pro-inflammatory astrocytes (Liddelow & Barres (2017)), this thesis will focus on the expression of the pro-inflammatory astrocytes (termed

"A1") and the consequent signaling pathway of NF-κB activation that occurs when signal transducer and activator of transcription 3 (STAT3) is downregulated. It is important to note that astrocytes are heterogenous and exist in a mixture of "normal," pro-inflammatory, and anti-inflammatory populations at any given time, where the dominant expressed population is determined by brain injury type (Li et al. (2019); Liddelow & Barres (2017)). With an upregulation of C3 associated with A1 astrocytes, neurons release gliotransmitters which promote calcium channel activity at the astrocytic end feet through increases of the expression of L-type voltage-gated calcium channels (VOCCs). As inflammation progresses from acute to chronic over time, there is an accumulation of activated microglia sheath followed by an additional layer of pro-inflammatory reactive astrocytes (Kozai et al. (2015a)).

1.2.0.4 Neuronal Loss

Neurotoxic reactive astrocytes have lost the ability to support neuronal homeostasis and contribute to neuronal death, potentially by releasing increasing amounts of glutamate in the microenvironment (excitotoxicity). Spillover of excess glutamate may also accompany glutamate receptor desensitization and extracellular matrix (ECM) degradation of neuronal processes (Bikbaev et al. (2015)). Glutamate receptor desensitization and ECM degradation affects the morphology and firing ability of neurons by causing an initial hyperexcitability response in firing that eventually leads to hypoexcitability (Bikbaev et al. (2015); Salatino et al. (2018, 2019)). To understand the importance of circumventing neuronal loss and its role in enhancing chronic probe stability, astrocyte function must be understood and used to maintain healthy bi-directional communication between neurons and astrocytes.

1.3 Astrocyte Function

1.3.1 Overview of Astrocyte Physiology

Astrocytes are the most abundant glial cell and play an important role in brain homeostasis. Astrocytes dictate circuit remodeling and contain a large number of localized G-protein coupled

receptors (GqGPCRs) on their processes that allows them to sense and react to exogenous agonists (Agulhon et al. (2013); Porter & Mccarthy (1995a,b)) and neurotransmitters released from presynaptic clefts (Agulhon et al. (2013); Kang et al. (1998); Perea & Araque (2005,?)). These receptors are organized as a trio of subunits, in which phosphorylation occurs on the gamma subunit by adenosine tri-phosphate (ATP), changing the conformation of the receptors, which either allows or prohibits a signaling cascade to occur in response to change in the astrocyte's microenvironment. Gliotransmitters (ATP, glutamate, and D-serine) that are released from neurons, can cause an increase in the internal calcium level in astrocytes, which then causes an increase in neuronal ionotropic glutamate receptor (iGluR) activity on neurons from astrocytic-released glutamate (Agulhon et al. (2013)). Depolarization across the astrocytic plasma membrane causes an influx of $[Ca^{2+}]$, which activates voltage-dependent calcium channels.

The discovery of this feedback loop suggests that astrocytes modulate neuronal activity, supporting the tripartite synapse theory in which pre- and post-synaptic neuronal compartments combine with the astrocyte to act as a single functional synapse. Even though there is evidence (Agulhon et al. (2013); Perea & Araque (2005); Salatino et al. (2018); Shigetomi et al. (2010)) that supports that astrocytic GqGPCR phosphorylation and activation by ATP increases intracellular astrocytic calcium, the exact pathways in which astrocytes release gliotransmitters is unclear. It is possible that the gliotransmitters released by astrocytes act on either the presynaptic or extrasynaptic ionotropic receptors of neurons (Agulhon et al. (2013)). However, it is evident that bidirectional communication occurs between astrocytes and neurons and that the change of astrocytic $[Ca^{2+}]$ affects astrocytic function.

Activation of calcium sensitive enzymes and proteins manages the uptake and redistribution of potassium (K^+), glutamate, GABA, glycogen metabolism and neuroactive substances that regulate the neuronal microenvironment and affect neuronal synaptic activity. Evidence (Agulhon et al. (2013); Kang et al. (1998); Porter & Mccarthy (1995a)) supports that change in $[Ca^{2+}]$ affects cytoskeletal structure, which has a downstream effect on astrocytic genetic expression. These observations implicate that astrocytic calcium from activated calcium voltage channels mediate

glutamic release, which effects long term excitotoxicity. It is possible that a change in calcium-dependent astrocytic genetic expression may affect long-term neuronal health and synaptic activity. To better understand the role of calcium channel activity in astrocytes, as it pertains to the health and firing of neurons, we must investigate the form and structure of activated calcium channels of astrocytes.

1.3.2 Role and Classification of [Ca^{2+}] Channels

Calcium is a ubiquitous second messenger involved in many signaling pathways including membrane electrical currents and electrophysiology (Ben-johny & Yue (2014)). It also plays a critical role in activation of astrocytes and consequent communication between astrocytes and neurons. In order to properly identify the type of calcium channels that become upregulated in the presence of reactive astrocytes, there must be an understanding of the difference in structure and function of calcium voltage gated channels, especially since each family has different channel blockers. In the event that this body of work determines that the upregulation of calcium channel expression does play a key role in the activation of astrocytes as it pertains to neurotechnology, it will be important to know and understand the antagonists of the calcium channels responsible. **Table 1** summarizes the genes, structure, function and antagonists of voltage gated calcium channels.

It is also important to note that spontaneous spikes in calcium concentration have occurred on the soma of astrocytes in basal conditions, without the observation of elevated neuronal activity (Agulhon et al. (2013)). Because this observation that calcium channels expressed on the soma of astrocytes are not the channels responsible for communicating with neurons, but rather the channels located on the astrocytic feet processes (Shigetomi et al. (2010)), it is important to identify L-type calcium channels in cortical astrocytes on their processes. In the next section, I will further explore the significance of proper calcium channel identification in astrocytes, as it pertains to the proteomic shift from normal to reactive cytoarchitecture.

Table 1.1: Summary of the types of Calcium voltage gated channels, involving structure and function. Hs is Homo sapiens (human), Mm is Mus musculus (mouse), and Rn is Rattus norvegicus (rat) genes.

Channel (α_1 subunit name)	**Genes** (Catterall et al., 2019)	**Channel Blocker** (Catterall et al., 2019)	**Type** (Catterall et al., 2019; Putney et al., 2018)	**Structure** (Putney et al., 2018; Zamponi et al., 2010)	**Location and Function** (Talley et al., 1999; Zamponi et al., 2010)
$Ca_v1.1$	CACNA1S (Hs), Cacna1s (Mm), Cacna1s (Rn)	diltiazem, verapamil	L-type, long lasting, high voltage activated (HVA)	$\alpha_2\delta$, β, γ	Hetero multimer that uses the α_1 subunit as its pore forming unit, which co-assembles with the β, $\alpha_2\delta$ and sometimes γ units. The $Ca_v1.X$ family is found in myocytes, smooth and skeletal muscle, bone and cardiac muscles. They are also found on the dendritic spines of neurons and on the astrocytic feet of reactive astrocytes.
$Ca_v1.2$	CACNA1C (Hs), Cacna1c (Mm), Cacna1c (Rn)				
$Ca_v1.3$	CACNA1D (Hs), Cacna1d (Mm), Cacna1d (Rn)	verapamil			
$Ca_v1.4$	CACNA1F (Hs), Cacna1f (Mm), Cacna1f (Rn)	diltiazem, verapamil			

Table 1.1: (cont'd)

Channel (α_1 subunit name)	**Genes** (Catterall et al., 2019)	**Channel Blocker** (Catterall et al., 2019)	**Type** (Catterall et al., 2019; Putney et al., 2018)	**Structure** (Putney et al., 2018; Zamponi et al., 2010)	**Location and Function** (Talley et al., 1999; Zamponi et al., 2010)
$Ca_v2.1$	CACNA1A (Hs), Cacna1a (Mm), Cacna1a (Rn)	ω-conotoxin MVIIC (peptide)	P-type, purkinjie, HVA ; Q-type, HVA	$\alpha_2\delta, \beta$, possibly γ	The $Ca_v2.X$ family is found in the Purkinje neurons in the cerebellum, while $Ca_v2.2$ is found throughout the peripheral nervous system.
$Ca_v2.2$	CACNA1B (Hs), Cacna1b (Mm), Cacna1b (Rn)	ω-conotoxin GVIA, ω-conotoxin MVIIC (peptides)	N-type, neural, HVA	$\alpha_2\delta/\beta_1,\beta_3,\beta_4$, possibly γ	
$Ca_v2.3$	CACNA1E (Hs), Cacna1e (Mm), Cacna1e (Rn)	Ni^{2+}	R-type, residual, intermediate voltage activated	$\alpha_2\delta, \beta$, possibly γ	

Table 1.1: (cont'd)

Channel (α_1 subunit name)	**Genes** (Catterall et al., 2019)	**Channel Blocker** (Catterall et al., 2019)	**Type** (Catterall et al., 2019; Putney et al., 2018)	**Structure** (Putney et al., 2018; Zamponi et al., 2010)	**Location and Function** (Talley et al., 1999; Zamponi et al., 2010)
$Ca_v3.1$	CACNA1G (Hs), Cacna1g (Mm), Cacna1g (Rn)	Ni^{2+}	T-type transient, low voltage activated	$\alpha_2\delta, \beta$, possibly γ	$Ca_v3.1$ is found in Inferior olivary, thalamic relay neurons, thalamic reticular neurons, Purkinje cell layer of the cerebellum, the bed nucleus of the stria terminalis, the claustrum subthalamic nucleus, amygdala, cerebral cortex, rostral hypothalamus, brainstem, and spinal cord.
$Ca_v3.2$	CACNA1H (Hs), Cacna1h (Mm), Cacna1h (Rn)				$Ca_v3.2$ is found in the sensory ganglia, pituitary, dentate gyrus, granule neurons, thalamic reticular neurons, olfactory tubercles, and basal ganglia.
$Ca_v3.3$	CACNA1I (Hs), Cacna1i (Mm), Cacna1i (Rn)				$Ca_v3.3$ is found in thalamic reticular neurons, subthalamic nucleus, and basal ganglia.

1.3.3 Signaling Pathway Activation in the Identity of Reactive Astrocytes

In 2001, Kajihara et al. observed that when the brain was subjected to ischemic damage, glycogen and glucose accumulated in the brain immediately after infarction, which was subsequently followed with the disappearance of glycogen stores, fibril scarring and the appearance of a more hypertrophied morphology (Kajihara et al. (2001)). They concluded that injury type could influence the cytoarchitecture of reactive astrocytes, and that there was more than one kind of reactive astrocyte. Following this observation, it has been demonstrated that if STAT3 is deleted in astrocytes, reactive gliosis results (Hashioka et al. (2011); Herrmann et al. (2008); Okada et al. (2006)), reinforcing further inflammation (Li et al. (2019)). Other studies have shown that the phosphorylation of NF-κB initiates CNS pathogenesis (Brambilla et al. (2009); Crosio et al. (2011); Dvoriantchikova et al. (2009)), suggesting that the activation of STAT3 initiates the release of neurotrophic factors and that NF-κB activation releases neurotoxic factors. In a separate study where Cheli et al. subjected cortical astrocyte culture to mechanical trauma, their enzyme-linked immunosorbent assay (ELISA) revealed the presence of chemokines IL-1β, IL4, IL6, IL10, IL12, IL17A, IFN-γ, TNFα, TGFβ1, MCP-1, MIP-1a and MIP-1b in the culture supernatant (Cheli et al. (2017)), implicating the phosphorylation of NF-κB (Li et al. (2019)) as a root mechanism (Liu et al. (2017)). In conclusion, literature (Brambilla et al. (2009); Crosio et al. (2011); Dvoriantchikova et al. (2009); Cheli et al. (2017); Hashioka et al. (2011); Herrmann et al. (2008); Kajihara et al. (2001); Li et al. (2019); Liu et al. (2017); Okada et al. (2006)) suggests the hypothesis that the type of damage that occurs at the implantation site of probes may initiate the NF-κB signaling pathway that converts normal to neuroinflammatory reactive astrocytes. Because Cheli et al. used verapamil, consequently decreasing the influx of calcium in cortical astrocytes (Cheli et al. (2017)), it has also been determined that these reactive astrocytes contain L-type voltage gated calcium channels, because verapamil is the only calcium channel blocker that can act as an antagonist for the $Ca_v1.X$ family (Catterall et al. (2019)). To further understand the impact of neuroinflammatory reactive astrocytes in the brain microenvironment, and the activated signaling pathways responsible for its change, I will investigate the impact of genetic changes to neurotoxic reactive astrocytes.

1.4 Evidence for Altered Gene Expression in Reactive Astrocytes

Astrocyte homeostasis is vital to neuronal function. When brain injury occurs, work from Ben Barres' group suggests that astrocytes either become neurotoxic (A1) or neuroprotective (A2) (Batlle & Labarta (2002)). A1 releases neurotropic factors such as BDNF, VEGF, but also inflammatory factors interleukin–1 beta (IL-1β), tissue necrosis factor alpha (TNFα), and nitric oxide (NO), etc. One biomarker that Liddelow et al., discovered to be highly upregulated and unique to the A1 phenotype, is complement component 3 (C3), (Liddelow & Barres (2017)) which has also been observed to be upregulated surrounding implanted electrodes in our RNAseq data (Gregory et al. (2021)). These extracellular molecules may activate Ca^{2+} channels as additional possible biomarkers for device-reactive astrocytes, as they are known to contribute to many neurodegenerative diseases and alter synaptic transmission (Li et al. (2019)). Interestingly so, literature has given evidence of altered gene expression of many commonly shared biomarkers concerning neurodegeneration and probe implantation (Ereifej et al. (2011)). Ereifej et al.'s work established difference in the amount of glia scarring between electrode materials, the difference of GFAP and MAPK expression of these materials (Ereifej et al. (2011)) and highlighted that micropatterning electrodes could decrease inflammatory signaling and encourage directional growth (Ereifej et al. (2013)). Our studies corroborate these findings upon observing a change in ion channel expression and function pre and post implantation (Salatino et al. (2019)), while demonstrating change in gene differential expression in tissue near and far from the probe (Thompson et al. (2021)). This leaves unanswered questions about how tracking differential expression of explanted tissue could give clues about FBR response to probes. It also suggests that monitoring astrogliosis biomarkers such as glial fibril acid protein (GFAP) alone, is not enough.

1.5 Gaps in Existing Knowledge of Astrocytic Foreign Body Response to Implantable Neurotechnology

Typically, GFAP or vimentin from post-mortem rat brain tissue, is used to measure FBR. However, given that GFAP expression is mainly conserved in mammals with limited expression in

other species (Liddelow & Barres (2017)) and that it can be expressed under normal physiological conditions (Boroujerdi et al. (2009)), literature (Liddelow & Barres (2017)) suggests that novel biomarkers should be investigated. Since the 1970's, it has been discovered that reactive astrocytes play an important role in most neurodegenerative diseases (Liddelow & Barres (2017)), and within the last 20 years, researchers have characterized reactive astrocytes into distinctive phenotypes (Li et al. (2019)). When the brain was subjected to injury that caused ischemia, Kajihara et al., observed that astrocytes lost normal function, responding to the environment by releasing neurotrophic factors (Kajihara et al. (2001)). Because of this and similar observations of "neuroprotective astrocytes" that behaved differently from the type of reactive astrocytes that was initially observed, in 2012, Zamanian et al., purified reactive astrocytes, profiling two different reactive phenotypes that were induced by neuroinflammation or cerebral ischemia (Zamanian et al. (2012)). Although Zamanian et al. details an exhaustive transcriptome of these two reactive types, there is no known data detailing the transcriptome of astrocytes in response to electrode materials. In addition, Cheli et al., observed astrocytes exposed to high levels of glutamate, K^+, and ATP, increased intracellular calcium, consequently activating calcium channel expression. Silencing L type calcium channels, using verapamil, attenuated these concentrations and astrogliosis, suggesting that these specific Ca2+ channels play a critical role in the activation of astrocytic inflammation signaling pathways (Cheli et al. (2017)). Characterizing the reactive astrocyte response to probes will give the field new insights about the characteristics of probe design which either minimize FBR or improve signal to noise ratio (SNR).

In summary, this research is novel because it is: **(1) bridging a knowledge gap about the functional effects of astrocyte reactivity by assessing changes in gene expression in a model of the tissue response to electrode materials; (2) potentially identifying uncovered biomarkers of astrocyte reactivity that should be investigated to measure the FBR to probes via RNAsequencing; and (3) providing insight on how probe design features can impact astrogliosis, potentially providing a new avenue to improve probe stability**. The purpose of the work in this dissertation is to elucidate the change in function and genetic identity of reactive astrocytes in

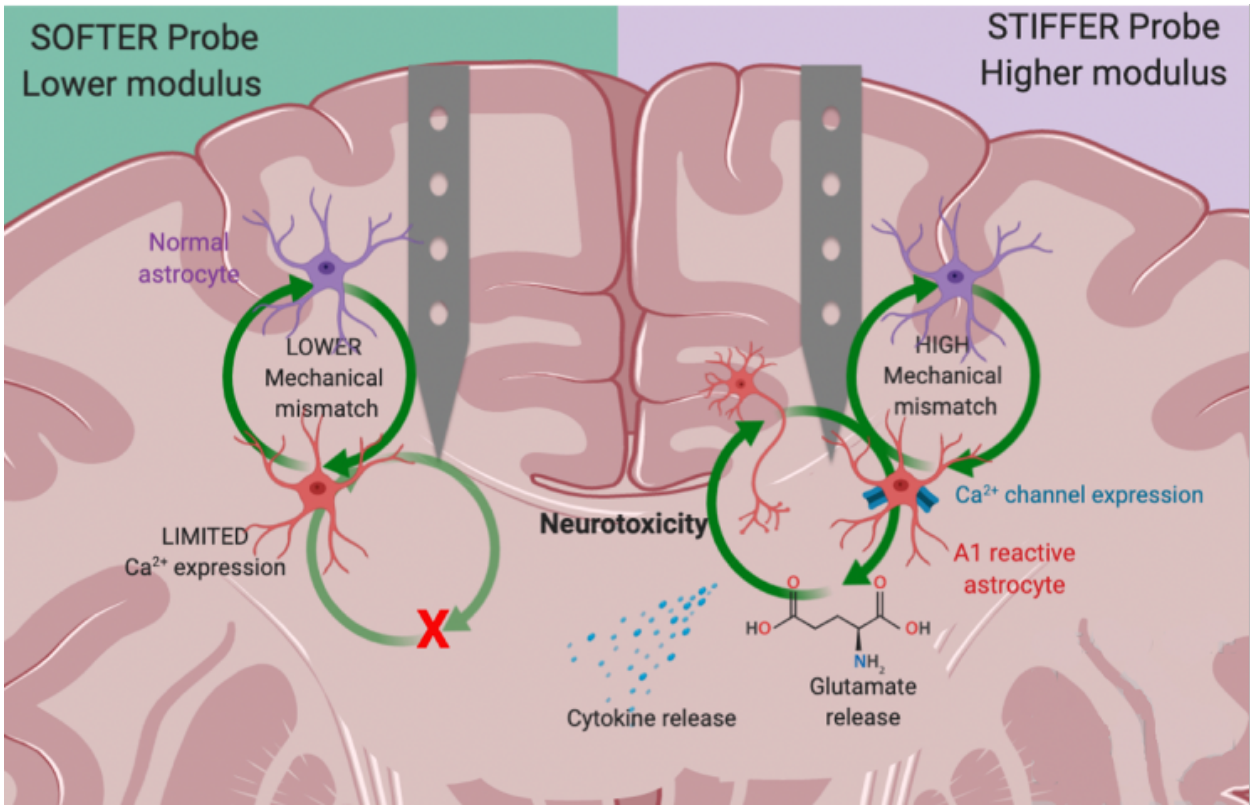

Figure 1.2: Illustrated summary of the hypothesized response to insertion trauma, mechanical mismatch and BBB breach

response to implantable neurotechnology. The overarching hypothesis is illustrated in **figure 1.2**.

In chapter 2, I will then explore surface modification techniques used to classify and characterize sample surfaces and biomaterials. I will emphasize the need to do because of the current large design space. I will then delve deeper into the literature summarizing characteristics of next generation probes, detailing the research successes and limitations.

CHAPTER 2

PATHOLOGICAL RESPONSE CREATES LARGE DESIGN SPACE WITHIN THE FIELD

2.1 The Brain is Heterogenous

2.1.1 Uniqueness and Complexity Gives Rise to Varying Measured Biomechanics

Unlike the extracellular matrix (ECM) found elsewhere in the body, brain ECM is made up of brain parenchyma, that consists of proteoglycans, and glycosamioglycans such as hyaluronic acid, meaning the mechanical properties of the functional tissue are governed by these macromolecules (Quail & Joyce (2017)). These building block molecules include those produced by astroglial cells, have mechano-sensing abilities which, are maintained through cell-to-cell communication, and gap junctions (Budday et al. (2017)) meaning brain biomechanics are dependent on these junctions. In order to completely understand brain signaling, mechanical properties of the environment and its effect on cells and tissues must be studied, manipulated, and characterized. However, it has been difficult to characterize the mechanical properties of normal brain, and literature characterizing brain tissue mechanical properties widely vary. A myriad of tissue preparation methods (Dyson et al. (2017); Lippert et al. (2004); Shen et al. (2006)), temperature conditions (Budday et al. (2017); Jin et al. (2013); TAMURA et al. (2007)), postmortem times and testing methods (Jin et al. (2013); Lippert et al. (2004); Luque et al. (2016)), such as rheometry (Green et al. (2008); Pogoda et al. (2014); Vappou et al. (2007)), magnetic resonance elastography (MRE) (Atay et al. (2008); Green et al. (2008); Vappou et al. (2007)), shear wave elastography (Collection et al. (2018)) and atomic force microscopy (AFM) (Collection et al. (2018); Luque et al. (2016); Pogoda et al. (2014)), are used, resulting in a range of values that vary by four orders of magnitude, as observed in an exhaustive list **(table 2.1)**.

Table 2.1: Literature summarizing measured brain biomechanics over the last 25 years. Important material property terms are listed: Elastic (Young's) modulus: measured resistance in response to applied stress on an object. Storage modulus: measure of material elastic response as stored energy. Loss modulus: measure of material viscous response as energy dissipated as heat. Nominal stress: force applied on an area, divided by the original area (measured area before deformation). Shear stress: force applied on an area, divided by the deformed area (measured area after deformation). Shear modulus: ratio of shear stress to shear strain.

Brain Mechanical Properties (Bilston, 2011)				
Brain Region	**Mechanical Property Measured**	**Animal Model Sample**	**Value**	**Sample prep/Methods**
Brain parenchyma, subgyral white matter, cortex	Elastic Modulus	Hydrocephalic human brain	584.4 N/m^2	CT scans and mathematical modeling using biphasic continuum (Taylor and Miller, 2004)
Grey and white matter	Storage Modulus G' Loss Modulus G"	Human brain	3.1 ± 0.1 kPA G' grey matter 2.7 ± 0.1 kPA G' white matter 2.5 ± 0.2 kPA G" grey matter 2.5 ± 0.2 kPA G" white matter	Quantitative mapping of response to mechanical stimulation via MRI -Magnetic resonance elasticity (MRE) and Rheometry (Rh) (Green, Michael and Bilstone, Lynne and Sinkus, 2008) using phantom MR

Table 2.1: (cont'd)

Brain Mechanical Properties (Bilston, 2011)				
Brain Region	**Mechanical Property Measured**	**Animal Model Sample**	**Value**	**Sample prep/Methods**
Brain sliced samples – no specific area indicated	Dynamic modulus Loss Modulus	Adult porcine brain	130-1500 Pa 35-800 Pa	Adult porcine brains were kept intact in skulls and refrigerated at 4°C for 2 days prior to purchase. Meninges were removed and the brain was coated with a light silicon oil at 37°C to prevent dehydration. Rotational tests were performed on 50mm diameter and 4mm thick samples. Oscillary, compression, and relaxation rheological tests were performed (Shen, 2006)

Table 2.1: (cont'd)

Brain Mechanical Properties (Bilston, 2011)				
Brain Region	**Mechanical Property Measured**	**Animal Model Sample**	**Value**	**Sample prep/Methods**
White matter from corona radiata	Shear Storage Modulus G' Loss Modulus G"	6-8 month old porcine brain	Freq – 0.1 Hz, 390 ± 180 Pa G', 75 ± 25 Pa G" Freq – 1 Hz, 465 ± 180 Pa G', 94 ± 30 Pa G" Freq – 10 Hz, 650 ± 130 Pa G', 190 ± 40 Pa G" Freq – 80 Hz, 1150 ± 150 Pa G', 910 ± 155 Pa G"	Normal porcine brains obtained from slaughter house and stored at 4°C for 24-48 hours. Cylindrical samples were excised and placed in 4°C rheometer chamber. MRE studies were also conducted at higher frequencies (Vappou et al., 2007)
Human meningioma, metastatic lymphoma, glioma, mouse brain and mouse tumor	Steady state modulus	Human and murine	3.97 ± 3.66 kPa to 1.56 ± 0.75 kPa, meningiomas to mouse brain, respectively 2.75 ± 1.40 kP, human glioma, and 2.10 ± 0.57 kPa for metastatic lymphoma	Resectioned human brain tumors with indentation tests performed within 3-4 hours after sample collections. Samples were on iced prior to mechanical testing (Dyson et al., 2017)

Table 2.1: (cont'd)

Brain Mechanical Properties (Bilston, 2011)				
Brain Region	**Mechanical Property Measured**	**Animal Model Sample**	**Value**	**Sample prep/Methods**
Meningiomas, low-grade gliomas, high-grade gliomas and metastasis	Young's modulus	Human	33.1 ± 5.9 kPa, 23.7 ± 4.9 kPa, 11.4 ± 3.6 kPa and 16.7 ± 2.5 kPa for meningiomas, low-grade gliomas, high-grade gliomas and metastasis respectively	Shear wave elastography (SWE) (Chauvet et al., 2018)
Cortex and hippocampus	Equilibrium modulus	Murine	0.13 ± 0.04 kPa for the cortex and 0.09 ± 0.015 kPa for the hippocampus (for Poisson ratio = 0.35)	Micro indentation combined with optical coherence tomography (OCT) (Lee et al., 2011)
Primary glioblastomas and normal murine brain	Young's Modulus	Human and murine, LN229 cells	Single cell LN229 ranged from 200 to 2000 Pa. LN229 cultured in polyacrylamide gels ranged from 300-1400 Pa. Normal mouse brain averaged 390 Pa, fresh glioma averaged 360 and frozen glioma averaged 200 Pa for young's modulus.	Normal brain tissues were punched into discs and glued to rheometry plates for macroscopy rheometry. For single cell stiffness, an AFM was used (Pogoda et al., 2014)

Table 2.1: (cont'd)

Brain Mechanical Properties (Bilston, 2011)				
Brain Region	**Mechanical Property Measured**	**Animal Model Sample**	**Value**	**Sample prep/Methods**
Corona	Young's modulus	Bovine, 16 month old	White matter average modulus is 1.895 kPa±0.592 kPa, while gray matter was 39% stiffer with an average modulus of 1.389 kPa±0.289 kPa.	Indentation of 5 mm thick slices, within 6 hours postmortem, performed at room temperature (Budday, Silvia and Nay, Richard and de Rooij, Rijk and Steinmann, Paul and Wyrobek, Thomas and Ovaert, 2015)
Corpus callosum, corona radiata, basal ganglia, and cortex	Nominal stress, shear stress, elastic shear stress, shear modulus,	Human	Shear moduli ranges from 0.3-0.38 kPa in shear, 0.4-0.5 in compression and 0.3 to 0.35 kPa in tension for the corpus callosum.	Whole brains were collected from cadavers within 24 hours postmortem and kept at 3oC in PBS at all times. Shear, compression, and tension loading modes were applied to 1cm thick slices within 48 hours of receiving samples. Constitutive modeling was used to determine values (Budday et al., 2017b)

Table 2.1: (cont'd)

Brain Mechanical Properties (Bilston, 2011)				
Brain Region	**Mechanical Property Measured**	**Animal Model Sample**	**Value**	**Sample prep/Methods**
Cerebellum	Elastic moduli	Murine, 2-3 months old	Elastic moduli of 294 ± 74 and 454 ± 53 Pa, of white and gray matter respectively	Brain tissue slices using scanning force microscopy (SFM) with a 20 µm radius spherical indenter(Christ et al., 2010)
Hilus(H), Subgranular zone (SGZ), Granule cell layer (GCL)	Elastic moduli	Murine	Hilus (49 ± 7 Pa) and Subgranular zone (58 ± 8 Pa) and granule cell layer (115 ± 18 Pa)	A vibratome generated 400µm hippocampal slices from mice within 1 hour of sacrifice and then embedded in 0°C cutting solution. AFM indentation measurements were performed immediately afterwards for 1 hour (Luque et al., 2016).
Cerebellum and cortex	Shear modulus	Murine	Cerebellum (2.11 ± 1.26 kPa, 3.15 ± 1.66 kPa, 3.71 ± 1.23 kPa) and cortex (4.06 ± 1.69 kPa, 6.14 ± 3.03 kPa, 7.05 ± 3.92 kPa) at 5, 10, and 15 indentations/sec	Fresh lateral slices were removed from mice and all tests were performed using a custom 3D printed micro indenter within 6hrs post mortem (Macmanus et al., 2015)

Table 2.1: (cont'd)

Brain Mechanical Properties (Bilston, 2011)				
Brain Region	**Mechanical Property Measured**	**Animal Model Sample**	**Value**	**Sample prep/Methods**
Whole brain from live animals and brain slices (coronal sections) from anesthetized animals	Dynamic Shear modulus	Murine	12,000–19,000 Pa at 1200 Hz	MRE of coronal sections taken within 2 hours post mortem(Atay et al., 2008)
Sagittal, superior and inferior sections of the brain	Viscoelastic response due to shear	Bovine, less than 1 year old	50 Pa at 0 langragian shear strain to 150 Pa at 0.15 langragian shear, samples subject to 5 Hz	Brain samples were obtained immediately after being slaughtered and transported in a saline/serum solution at 0°C within 24 hours post mortem. Samples were loaded and attached to a stationary and moving plate within a temperature controlled chamber to simulate shaking (Darvish and Crandall, 2001).

Table 2.1: (cont'd)

Brain Mechanical Properties (Bilston, 2011)				
Brain Region	**Mechanical Property Measured**	**Animal Model Sample**	**Value**	**Sample prep/Methods**
Cortex, thalamus, corpos callosum (CC), corona radiata(CR)	Tension, compression and shear	Post mortem human subjects, 45-90 years old	Tensile stress at 50% strain for the cortex ranged from 2-8 kPa, for the thalamus 2-11, for the CC 2-10, and for the CR 2-15kPa. Compressive stress at 50% strain for the cortext ranged from 15-18 kPa, for the thalamus 9-21, for the CC 11-19, and for the CR 15-27 kPa. Shear stress at 50% strain for the cortex ranged from 0.5-1.7 kPa, for the thalamus 0.45-1.8, for the CC 0.6-1.8, and for the CR 0.8-1.8 kPa.	Brain was kept intact at 4oC before craniotomy was performed. All samples were kept at this temperature for an average of 4 days prior to testing. The specimens were glued to a fixed block of a mechanical loading apparatus before all 3 tests were performed (Jin et al., 2013).

Table 2.1: (cont'd)

Brain Mechanical Properties (Bilston, 2011)				
Brain Region	**Mechanical Property Measured**	**Animal Model Sample**	**Value**	**Sample prep/Methods**
Corona radiata and cerebral cortex	Compression, relaxation, and apparent elastic moduli	Porcine, 6 month old	Elastic moduli of 5.7, 11.9 and 23.8 kPa for a strain rate of 1, 10 and 50s^{-1}, respectively	Brains were kept in ice box immediately after death then stored in a freezer for 1hr to ease separation of pia matter. The samples were stored in a petri dish, in a refrigerator until mechanical testing was performed. Compression and indentation tests were performed via a mechanical loading machine (TAMURA et al., 2007).

Table 2.1: (cont'd)

Brain Mechanical Properties (Bilston, 2011)				
Brain Region	**Mechanical Property Measured**	**Animal Model Sample**	**Value**	**Sample prep/Methods**
White and gray matter slices of 12.7 mm in diameter	Young's Modulus Complex Shear Modulus	Lamb	White matter ranges from 0.467 at 100 kHz to 0.415 at 10 MHz for Poisson's ratio, 422.1 MPa to 1153 MPa for young's modulus, and 143.9 MPa to 376.9 MPa for storage modulus. Gray matter ranges from 0.476 to 0.404 for poisson's ratio, 422.1 MPa to 1153 MPa for young's modulus, and 143.9 MPa to 412.4 MPa for storage modulus.	Fresh brain tissue was packed into tubes and subjected to wave speeds of 1, 2.25, 5 and 10 MHz at 25-27°C within the tubes. Finite element models were used to calculate material properties. All measurements taken within 5 hours and 27 minutes after anesthetization (Lippert et al., 2004)

Table 2.1: (cont'd)

Brain Mechanical Properties (Bilston, 2011)				
Brain Region	**Mechanical Property Measured**	**Animal Model Sample**	**Value**	**Sample prep/Methods**
Transverse whole brain slices	Unconfined compression, shear stress, tensile stress at dynamic strain rates	6 month old porcine brain	Samples subjected to a strain range of 0-0.1 averaged an elastic modulus of 11.68 ± 3.78 kPa, a strain range of 0.1-0.2, averaged elastic moduli of 27.6 ± 5.93 kPa, and a strain range of 0.2-0.3, averaged elastic moduli of 43.75 ± 5.97 kPa.	Samples were collected 6h after death from slaughter house, and stored in physiological saline solution 4°C during transportation. Samples tested at room temperature. 10 mm diameter average samples with an average height of 15 mm were excised from the coronal area (Michael et al., 2014)
Annulus and cylindrical shaped corona radiata samples	Engineering stress, engineering strain	Adult bovine brain	Engineering stress ranged from 0-1000 kPa, peaking at catastrophic failure around 70% engineering strain.	Adult steers were harvested and the brain samples were excised and stored in artificial cerespinal fluid at 37°C within 4 hours postmortem. A modified split Hopkinsin pressure bar technique was implemented for mechanical testing (Pervin and Ã, 2009)

2.2 Researchers Respond with Next Generation Probe Designs

2.2.1 Surface Features Modifications and Strategies

Surface chemistry and topographical cues have received relatively lesser attention from the device design community than architecture and flexibility/ softness; nonetheless, their impacts are inextricably intertwined with the incorporation of new materials in next-generation designs. The surface variables that can be measured and controlled are: hydrophilicity, chemistry, and surface topography. Contact angle/wettability measures surface energy, spectroscopy determines chemical composition, and scanning probe technique characterizes micro-level topography **(figure 2.1)**. While there are no field-standard guidelines, contact angles measured ideally should be low, indicating high surface energy in the range of 40–80 dynes cm^{-1}. This is the range at which materials are hydrophilic enough to favor hydrogen bonding between the biomaterial surface and surrounding fluid over the hydrophobic interactions which favor protein adsorption (Harnett et al. (2007)). Foundational studies have reported the fundamental physical characteristics of the surfaces presented by materials commonly used in electrode design. Polyimide is a hydrophobic material (contact angle reported between 80–100°) with an associated high adsorption of proteins (Jr et al. (1993)). Nonetheless, it exhibits low cytotoxicity and hemolysis, in alignment with biocompatible materials that served as a benchmark in the study (Teflon®and Silastic®). Parylene-C is similarly hydrophobic and biocompatible, although plasma treatment can be used to render the surface hydrophilic (Chang et al. (2007)). Silicon has been shown to be comparatively less biocompatible (in terms of thrombogenicity) than its polymeric counterparts, Parylene and polyurethane (Weisenberg & Mooradian (2001)). SU-8, while generally regarded as a highly biocompatible polymer, reportedly displays similar hemocompatibility to silicon, with similar platelet reactivity and thrombogenicity (Weisenberg & Mooradian (2001)).

Specific surface cues have been observed to be especially amenable to neuronal growth and responsiveness (Farrukh et al. (2018); Mammadov et al. (2013); Yang & Narayan (2019)), and the dimensions of topo- graphical features are known to influence effects: optimal promotion of

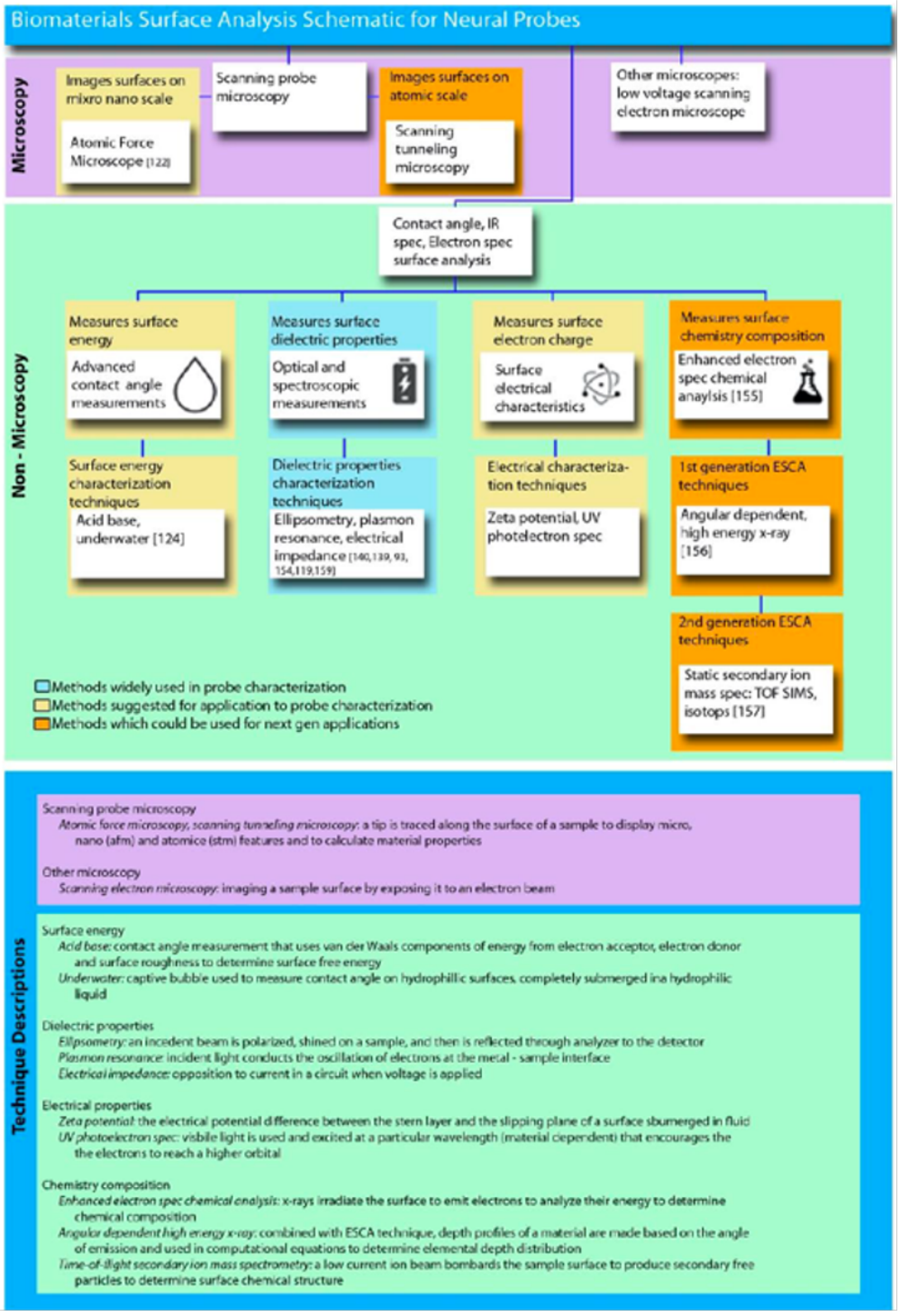

Figure 2.1: A systematic approach to choosing surface techniques for neural probe biocompatibility based on desired properties to be measured (Brinen & Melera (1972); Gardella & Hercules (1980); Hess et al. (2011); Kook et al. (2016); Kim et al. (2010); Kozai et al. (2015b); Pijolat & Hollinger (1981); Wade et al. (2013); Seymour & Kipke (2007); Ware et al. (2013); Zhong & Bellamkonda (2007))

neuronal growth occurs when the spatial pattern for controlled directionality matches the dimensions of neuronal growth cones(Basso et al. (2019)). Preliminary reports from Ereifej and colleagues in the Capadona lab suggest that nuanced topographical and architectural changes can impact the expression of pro- inflammatory factors surrounding neural implants. In an experiment where traditional planar probes were etched to form small, 200 nm high grooves across the length of the probe, tumor necrosis factor alpha (TNFα), nitric oxide synthase (NOS2), and a chroma- tin protein, high mobility group box 1 (HMGB1), were upregulated in the un-etched devices. The patterned probes showed a downregulation of the lipopolysaccharide binding receptor CD14 expression over a 2–4- week time-period which may suggest a trend towards increased regeneration as microglia and monocyte populations return to baseline. These results suggest that smooth planar shanks may create a more continuous expression of interleukin 1 beta (IL1β), resulting in prolonged BBB leakage, and potentially upregulated TNFα and NOS2 as a downstream consequence (Ereifej et al. (2018a)). Given the rationale for surface-mediated control of biocompatibility, numerous strategies have emerged in the field to influence biocompatibility through modifications to implanted electrode surface features **(figure 2.2)**. Biomimicry—making the device invisible to brain tissue by imitating its key features—is one strategy to address device failure and improve long term function and 'mask' the device from its surroundings. Biologically active materials such as L1 (neural adhesion molecule) have been coated on Parylene-C microwires and shown to decrease markers of apoptosis and astrogliosis at the injury site (Kolarcik et al. (2012)) and improve neuronal growth and survival around the implant (Azemi et al. (2011)). Alpha melanocyte stimulating hormone (Alpha-MSH) (He et al. (2007)) has also been proven to lower expression of markers of gliosis while chABC delivery likewise has been reported to reduce ionized calcium binding adaptor molecule (IBA1) and chondroitin sulfate (CS) expression (Mercanzini et al. (2010)). Recently, Oakes et al used a decellularized bovine astrocyte derived extracellular matrix (ECM), traditionally used in emergency rooms to promote wound healing, to coat Michigan-style arrays. The coating reduced the amount of astrogliosis, hemostatic activity, and macrophage activation in vitro (Oakes et al. (2018)). However, the short life time of the coating limits an effective response to chronic or long-term foreign body

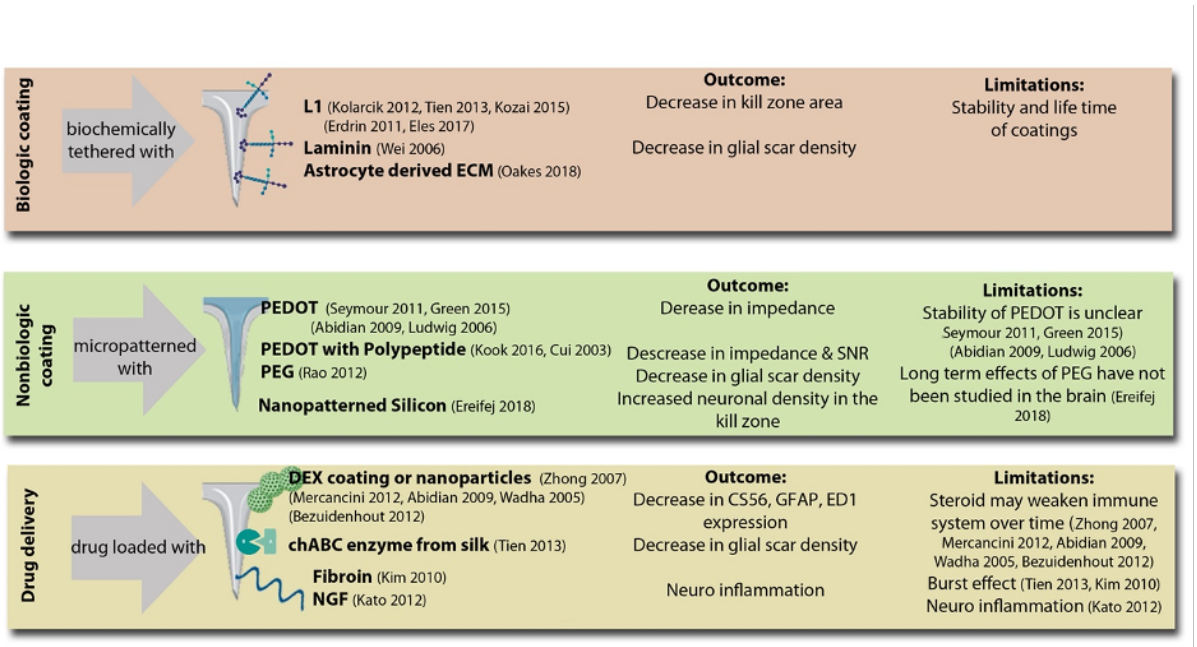

Figure 2.2: Next generation surface modification strategies with experimental outcomes and limitations (Abidian & Martin (2009); Bezuidenhout et al. (2013); Cui & Martin (2003); Eles et al. (2017); Ereifej et al. (2018b); Green & Abidian (2015); Kato et al. (2006); Kolarcik et al. (2012); Kook et al. (2016); Kozai et al. (2015a); Ludwig et al. (2006); Mammadov et al. (2013); Mercanzini et al. (2010); Oakes et al. (2018); Seymour et al. (2011); Tien et al. (2013); Wadhwa et al. (2006); Zhong & Bellamkonda (2007))

response.

Drug-eluting or drug-presenting surfaces are another avenue to modulate device-tissue integration. Dexamethasone (DEX) coated (Mercanzini et al. (2010)) and DEX loaded probes (Zhong & Bellamkonda (2007)) have been shown to decrease anti-chondroitin sulfate antibody (CS56), GFAP, and ED1 expression in surrounding tissue as well as reduce impedance by up to 25% for 9 d. However, there are also limitations surrounding long term tethering of biologically active molecules on these probes with reports of cracks in DEX film coatings at four weeks (Wadhwa et al. (2006)), and observations of the 'burst effect' (Abidian & Martin (2009)). Future improvements may include prolonged drug release, better drug adherence to the surface, and increased drug loading/release for enhanced efficacy (Wadhwa et al. (2006)). Despite these many advances, this large probe design space exists because of probe instability, hinting that implantable technology researchers lack a complete understand and about brain FBR.

2.3 Current Techniques Used to Evaluate FBR in Probes

To measure probe biocompatibility and astrocytic FBR, researchers often will measure the amount of GFAP or vimentin from post-mortem rat brain tissue, having GFAP identified and discovered as the key biomarker of astrogliosis since 1971 (Bignami & Dahl (1976)). However, Bignami et al. discovered that GFAP is not conservative across species, suggesting that it may not be the best biomarker for astrogliosis (Bignami & Dahl (1976)). Recent literature further highlights the complexity of reactive astrogliosis, suggesting that other novel biomarkers should be investigated. Since the 1970's, it has been discovered that reactive astrocytes play an important role in most neurodegeneration diseases (Liddelow & Barres (2017)), and within the last 20 years, researchers have characterized reactive astrocytes into distinctive phenotypes (Li et al. (2019)). When the brain was subjected to injury that caused ischemia, Kajihara et al., observed that astrocytes lost normal function, responding to the environment by releasing neurotrophic factors (Kajihara et al. (2001)). Because of this and similar observations of "neuroprotective astrocytes" that behaved differently from the type of reactive astrocytes that was initially observed, in 2012, Zamanian et al., purified reactive astrocytes, profiling two different reactive phenotypes that were induced by neuroinflammation or cerebral ischemia (Zamanian et al. (2012)). Although Zamanian et al. details an exhaustive transcriptome of these two reactive types, there is *no known data detailing the transcriptome of astrocytes in response to electrode materials.*

2.4 Innovation: Critical Knowledge Gap in the Field

Characterizing the reactive astrocyte response to probes will give researchers new insights about the characteristics of probe design which either minimize FBR or improve signal to noise ratio (SNR). Genetic and proteomic changes of reactive astrocytes in response to implantable neurotechnology, have yet to be fully understood to the point of mitigating long term device performance. In the following chapter, chapter 3, this body of work will add to the field via direct surface characterization of microelectrode array surface roughness and bending stiffness measurements. I will then corroborate my findings with how these features may influence the

identity and function of astrocytes in chapter 4, from a genomic and proteomic standpoint. Finally, I will address the implications of this work highlighted as future directions in the final chapter.

CHAPTER 3

ATOMIC FORCE MICROSCOPE CHARACTERIZATION OF THE BENDING STIFFNESS AND SURFACE TOPOGRAPHY OF SILICON AND POLYMERIC ELECTRODES

3.1 Introduction

Electrode arrays implanted intracortically have the ability to communicate with local neurons, allowing tetraplegic patients to regain motor function (Ajiboye et al. (2017); Hochberg et al. (2006, 2012); Kim et al. (2008); Simeral (2011)). However, neural signals decrease significantly after a year post implantation (Barrese et al. (2013); Chestek et al. (2011); Hochberg et al. (2012)), with chronic glial encapsulation hypothesized to be a culprit that drives neuronal death (Biran et al. (2005); Polikov et al. (2005); Salatino et al. (2017)). The mismatch in stiffness between rigid implants and soft brain tissue is believed to influence the degree of tissue response surrounding microelectrode arrays; therefore, researchers are designing soft and flexible next-generation devices as a means to mitigate intervention strategies (Thompson et al. (2019)). Initially, Young's modulus was believed to be an important determinant of the mechanical mismatch, but more recently, researchers have focused on bending stiffness, which is a property that incorporates both Young's modulus and device feature sizes. Bending stiffness has been estimated using mathematical modeling techniques which assign a value based on models of a cantilever beam, **figure 3.1** (Lee et al. (2005); Stiller et al. (2018); Subbaroyan et al. (2005)).

Surface topography may also influence reactivity, but topography is a material feature which has been given less attention in the literature in comparison to stiffness. Synergistically, topography and surface chemistry illustrate a surface's biocompatibility, and the degree to which cells may attach (Thompson et al. (2019)). Change in cytoarchitecture in cells over time may give researchers clues about chronic device performance. As detailed in Chapters 1 and 2 of this thesis, the cell to surface substrate interface must be investigated in to understand changes in device performance.

Atomic force microscopy (AFM) is a powerful technique with nanometer resolution that can

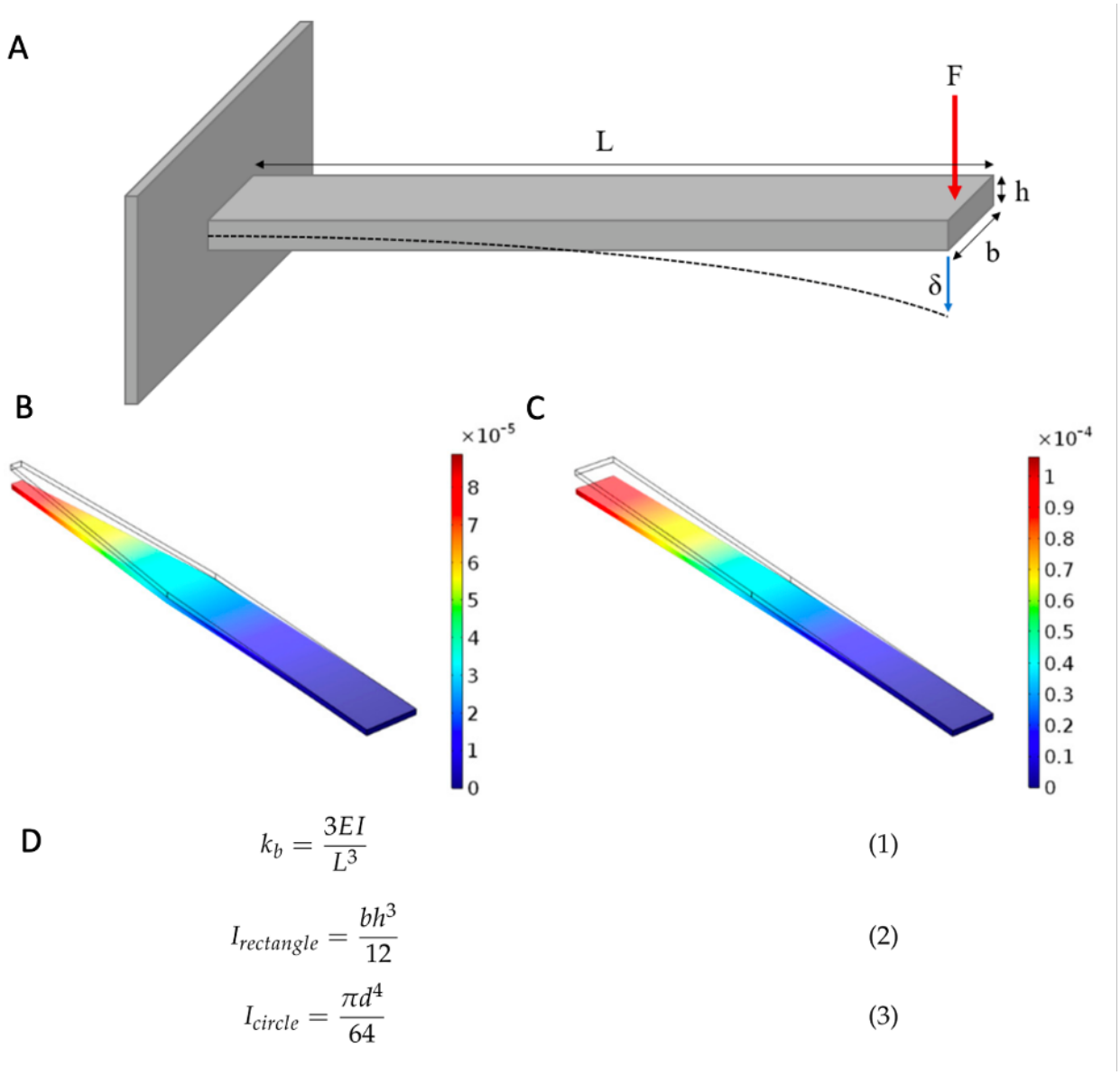

D

$$k_b = \frac{3EI}{L^3} \quad (1)$$

$$I_{rectangle} = \frac{bh^3}{12} \quad (2)$$

$$I_{circle} = \frac{\pi d^4}{64} \quad (3)$$

Figure 3.1: A) Diagram of a cantilevered beam. The beam is fixed on one end while a force on the opposite end produces a displacement, δ. Dimensions depicted are beam length, L, beam width, b, and beam thickness, h. Computer simulated bend tests. Cantilever bend tests were used to determine the percent difference between device geometries with tapered and symmetrical shanks. In this case, shank (B) featured a width of 290 µm and tapered to 65 µm starting halfway down the shank. Shank (C) featured a width of 234 µm, calculated based on the weighted average of width down the length of shank (B). Both shanks were 30 µm thick and 3 mm long. Colored scale bars indicate deflection in meters. (D) Equation (1) were calculated using average values of device width along the length of the shank. All devices were treated as having either rectangular cross sections with height, h, and width, b, or circular cross sections with diameter, d, affecting the way in which moment of inertia of the cross-sectional area was calculated (Equations (2) and (3) (Stiller et al. (2018))

measure surface roughness, use force mapping to give the change in modulus based on device features, and measure changes in modulus and bending stiffness in real time. This can allow researchers to be able to predict areas of mechanical damage, which could lead to device failure predictions (Barrese et al. (2013)). Bending stiffness in particular measures the electrode shank's propensity to move within the brain and can forecast the degree of gliosis that may occur (Stiller et al. (2018)). In this study, we perform a direct characterization of bending stiffness and surface topography on neural electrode arrays constructed from 3 different materials (silicon, polyimide, and parylene). We used AFM to measure the surface roughness of all device types, and then we directly measured the bending stiffness of suspended silicon Michigan array shanks. We determined the bending stiffness of silicon shanks by calculating the slope of the force curves created on various features down the length of the shank. We found nano-scale variation of topography roughness ranging from 27 nm to 1.6 μm, with the larger measurements corresponding to devices made of parylene. Direct measurement of the bending stiffness of silicon shanks varied from 0.29 to 0.32 N/m. Here, we add to the body of existing literature by directly measuring surface roughness and bending stiffness to corroborate estimated bending stiffness calculations and add to what is understood about device surface topography. To the best of our knowledge, this is the first report to detail these characteristics in these device types.

3.2 Methods

For each measurement, a Cypher S AFM (Asylum instruments, Santa Barbara California) was used to image each probe. The cantilever probes used in tapping mode in air to image topological features for surface roughness (rms) were 160AC-NA-10 silicon nitride cantilever probes, (k= 26 N/m, length= 160μm, F = 300 kHz). "RMS" surface roughness was calculated in the IGOR 6.37 software as the root mean square of nanoscale peaks and valleys in the imaging window of each sample surface imaged. The probes used to perform force curves were the ARROW-CONTR-10 silicon nitride probes with reflexive coating (k= 0.2 N/m , length = 450μm, width = 45μm, F = 14 kHz) (Nanoandmore USA) imaged in contact mode. All images were analyzed using the IGOR 6.37 software, where masking post image analysis was used to subtract surface impurities

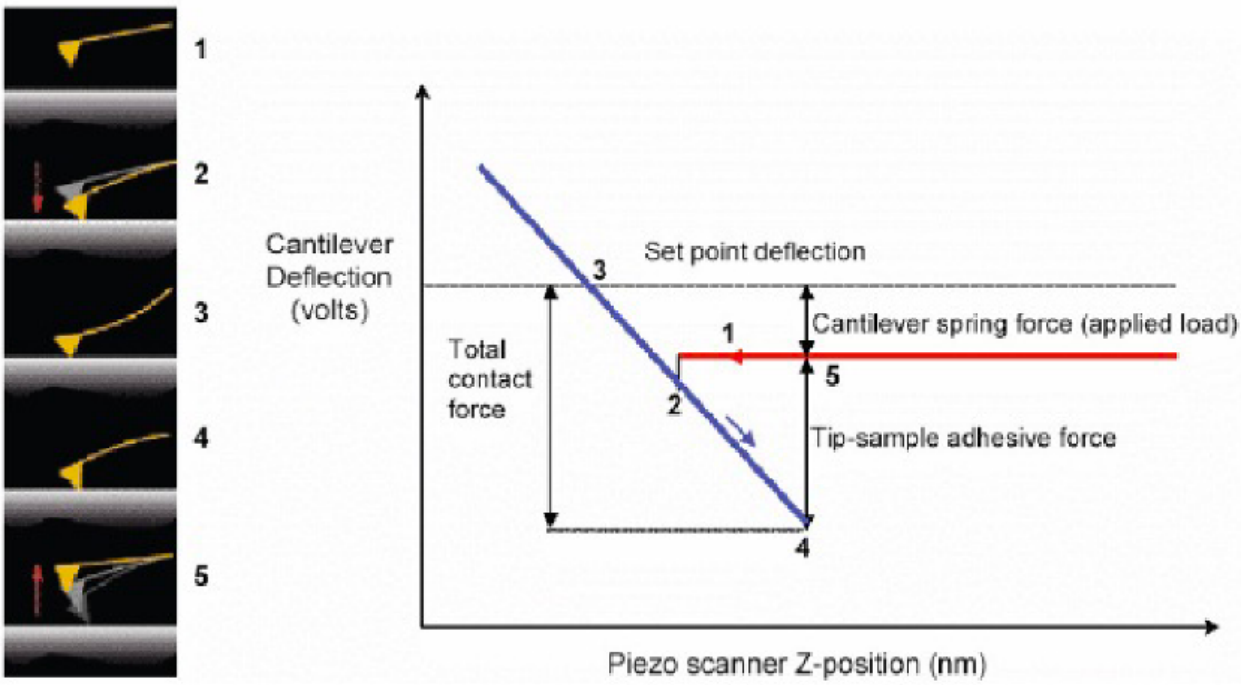

Figure 3.2: Force distance curve. Steps 1-2: cantilever tip is drawn to the service via attractive forces. Steps 2-3: Tip deflection occurs from initial contact and the slope that is used to measure stiffness forms. Steps 3-4: surface retracts. Steps 4-5: tip goes further past original deflection. The degree to which this occurs depends on surface viscoelasticity. Step 5: adhesion forces are disrupted, bring cantilever tip off (AZoNano (2012))

and debris artifacts from roughness measurements. Sample polyimide probes and parylene probes were supplied courtesy of Dr. John Seymour (University of Texas) and Dr. Wen Li (Michigan State University), respectively. Methodology for the fabrication processes are detailed here (Khurram & Seymour (2013)) and here (Lei et al. (2014)). Force curves were performed on individual Michigan array silicon shanks (5AA1: 3mm long, V673: 5 mm long, 5A9E: 3 mm long, all 50µm thick, Neuronexus) suspended horizontally from their Omnetics connectors, to create force maps. The slopes of the force curves were used to calculate bending stiffness (Butt et al. (2005)), illustrated in **figure 3.2**.

3.3 Results and Discussion

3.3.1 Surface Topography Roughness and Its Effects on Immune Response

Biomaterials have been established as the oldest area of concentration in biomedical engineering since the end of world war II, resulting in the abundance of materials, which often was used to create prosthetics for soldiers coming home from war. In the past century, our thought and focus on biomaterials, specifically implantable materials and bio-tissue interfaces, has shifted from bionert to a bioactive designs, as our understanding of the immune system grows (Abaricia et al. (2021)). This is also evident in the field of neural engineering as we have augmented the design space of recordable device implantable technology into three classes of next generation probes that alter immune response in some way (Thompson et al. (2019)). Consequently, there is literature (Abaricia et al. (2021)) that studies biomaterial features such as surface chemistry, energy, wettability, and roughness and how these physical properties affect immune system response. Hotckiss et al., demonstrated that increased roughness also accompanied increased macrophage activation but the combination of roughness and wettability also increased the presences of anti-inflammatory markers (Hotchkiss et al. (2016, 2017, 2018, 2019)). These findings support Ereifej et al.,'s work exploring the effects of nanopatterning microelectrode array surfaces for a decreased immune response (Ereifej et al. (2018b)). This body of literature also suggests that there is an ideal surface roughness range to achieve maximum cell attachment on silicon array probes. Here, we have imaged the surface and measured roughness of three electrode array materials, polyimide, parylene, and silicon, at nanometer resolution with the intention to predict tissue response outcomes, **figure 3.4, table 3.1**.

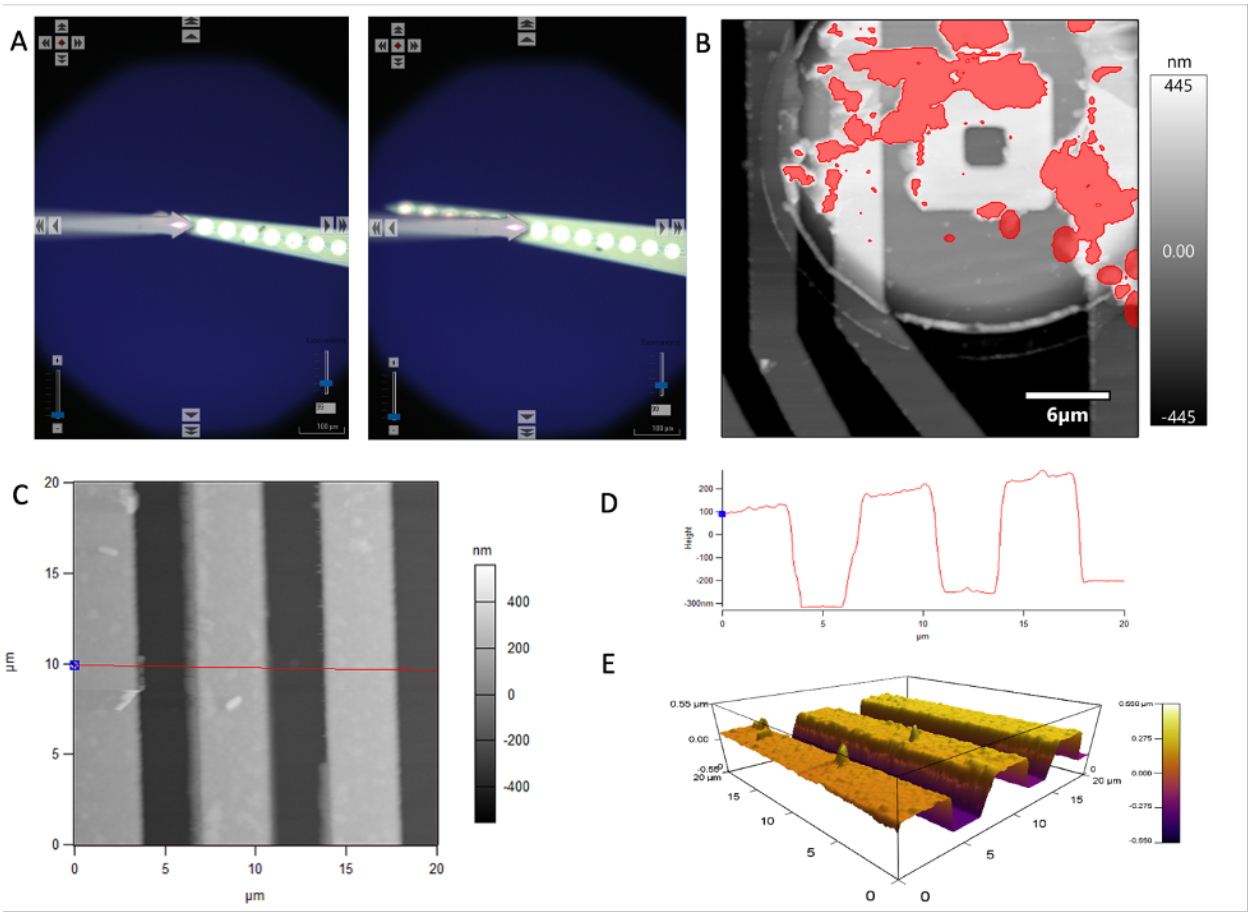

Figure 3.3: Surface roughness characterization of a single Neuronexus silicon probe. (A) Brightfield images highlighting nanometer resolution to measure all probe features and select specific features. Scale bar is 110µm. (B) Masking artifacts (highlighted in red) on a silicon recording device to accurately measure surface roughness. Scale bar is 6µm. Scale bar on the side indicates height of features based on gradient. (C) A 20 x 20µm topographical image of iridium traces and silicon troughs. Line draw through window gives height profiles of features, measured in (D). (E) 3D rendering of the silicon traces and troughs from (C).

Table 3.1: Summary of measured roughness rms for each probe material surface

Device Surface Roughness		
Probe Material	**Feature**	**RMS**
Polyimide A	Trace-trough (mid probe) Recording site Trace-trough (top of probe)	37.17 nm 1.22 µm 42.19 nm
Polyimide B	Trace-trough (mid probe) Recording site Trace-trough (top of probe)	17.89 nm 559.10 nm 680.50 nm

Table 3.1: (cont'd)

Device Surface Roughness		
Probe Material	**Feature**	**RMS**
Polyimide C	Trace-trough (mid probe) Recording site Trace-trough (top of probe)	47.10 nm 1.06 μm 212.57 nm
Silicon A	Trace-trough (mid probe) Recording site Trace-trough (top of probe)	215.97 nm 225.79 nm 371.14 nm
Silicon B	Trace-trough (mid probe) Recording site Trace-trough (top of probe)	27.32 nm 922.72 nm 1.22 μm
Silicon C	Trace-trough (mid probe) Recording site Trace-trough (top of probe)	489.21 nm 225.79 nm 1.215 μm
Parylene A	Trough Gold Trace	1.31 μm 1.43 μm
Parylene B	Trough Gold Trace	1.61 μm 1.55 μm

All images and image analysis were performed, quantified and analyzed on the AFM. The polyimide probes rms ranged from 17.89 nm to 1.22 μm, with an average rms of 430.71 nm. The silicon probes rms ranged from 27.32 nm to 1.22 μm, with an average rms of 497.16 nm. The parylene probes rms ranged from 1.31 μm to 1.61 μm, with an average rms of 1.48 μm. Although the softer and more flexible of the materials were polyimide and parylene, with parylene being the thinnest probes, it has the highest rms. Currently, 4 out of the 9 measured polyimide features meets Khan et al.,'s ideal range for cellular adherence, while only one feature on one silicon probe, and no parylene features meet this standard. However, this range was determined specifically for silicon material surfaces and does not consider all device properties and geometries for each individual probe material.

Further characterization methods including, force mapping, which are force distance curves taken at different features across a surface, can be used to determine the change in modulus, stiffness, bending stiffness or roughness across features (Butt et al. (2005)). When force maps are created, **figure 3.4**, it is possible to delineate between uncovered substrate and other protein

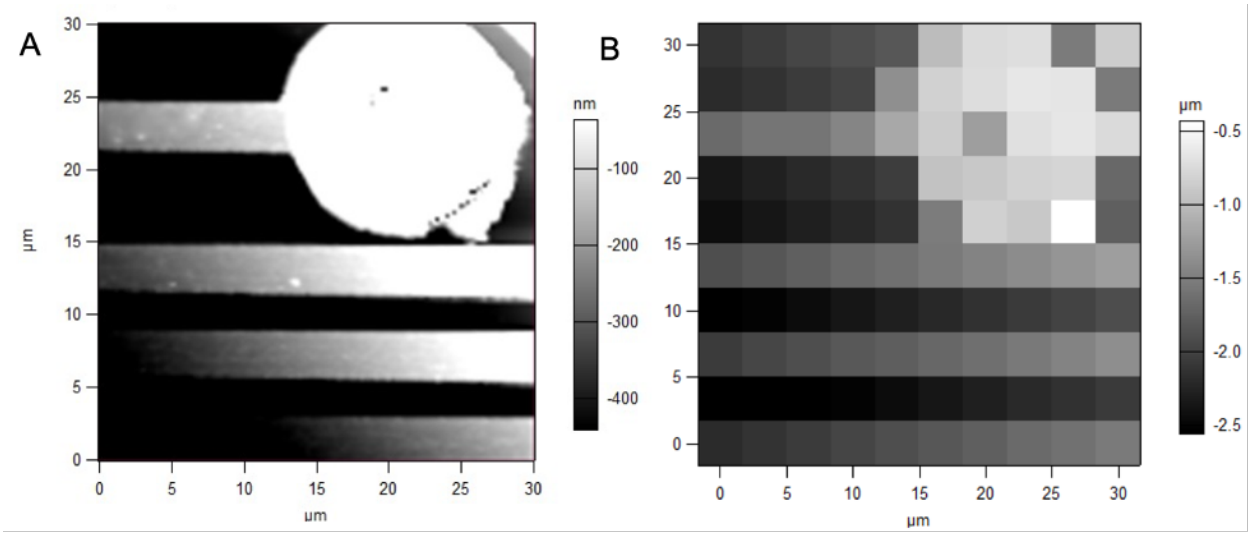

Figure 3.4: A) Topological view of a polyimide probe showing traces, troughs and a recording site in a 20 x 20 µm window. (B) Corresponding force map showing the change in height of these features in this image. Each square represents data that can be extracted in IGOR 6.37 to measure modulus, calculate bending stiffness (if material is suspended) and the characterize the distribution of materials on a surface. This can be a useful tool to predict cellular adhesion and points of probe failure

interactions on the surface of a cantilever tip. It is possible to measure or conduct adhesion studies of cells across different features in the substrate, which could be a useful measurement to predict where cellular adhesion is most likely to occur.

3.3.2 Implications of Directly Measured Roughness and Bending Stiffness

Although roughness and bending stiffness of device surfaces are important factors that affect immune response, they cannot solely be considered in isolation. In fact, the combination of sample, material properties, geometries and size synergistically affect immune response (Abaricia et al. (2021)). Cross-sectional area or elastic modulus cannot illustrate a complete roadmap of device properties and its effects on signaling: a device made from a soft material may be so large in dimension that it cannot flex with the pulsating brain (Stiller et al. (2018)). Conversely, a small device made from a material with a high Young's modulus may face the same issue (Stiller et al. (2018)). Khan et al.,'s work investigated biomaterial surfaces in general and found an ideal surface roughness range, Ra, which does not use root mean squared, that encouraged cortical neuron cell

adherence to silicon wafers, was 20 to 100 nm (Khan et al. (2005)). Focused on intracortical electrode arrays specifically, Stiller et al., performed a meta-analysis of histology results combined with estimated bending stiffnesses, coming to the conclusion that improved histological outcomes with respect to both GFAP intensity and neuronal nuclei (NeuN) density appeared to be mitigated when a device reached the 10-2 to 10-1 N/m bending stiffness range (Stiller et al. (2018)). This finding could serve as a threshold for optimal device stiffness to mitigate gliosis and neuronal death. However, the bending stiffness is based on a calculation, which provides only an estimate of the true value. As result, we decided to investigate the validity of these data by making a real time device characterization and comparing measurements to calculated results by performing several force curves on multiple features down the shaft of Neuronexus shanks connected to their Omnetics boxes **(figure 3.5)**.

Although these probes are suspended in air and will not summarize the biophysical conditions of the brain microenvironment, the measured deflection in space could model the micromotion Michigan arrays may experience in the ever moving, pulsating brain. These characterization measurements, **figure 3.5**, may serve as guiding principles for silicon device design.

The Neuronexus shank used for these force curves is 50 μm x 123 μm with a CSA of 6,150 μm^2, that has a bending stiffness range from 0.29 to 0.32 N/m. This calculated range, (8.7859x10^{-9}N / 3.0029x10^{-8}m) to (7.787x10^{-9}N / 2.437x10^{-8}m), is slightly higher than the 10^{-2} to 10^{-1} N/m, but is roughly twice the calculated stiffness values from Knaack et al., (Knaack et al. (2016)) while being roughly 3 times the CSA..

3.3.3 Implications of Measured Bending Stiffness to Astrogliosis and Genomic Change in Expression around the Probe

Stiller et al.,'s work stressed the correlation between device stiffness and immune response in concert with modulus and CSA (Stiller et al. (2018)), with increased astrocytes and neuronal nuclei, supports the idea that probe device design must integrate design features that limits chronic response. But what does this mean at the genomic level? Are their specific biomarkers that

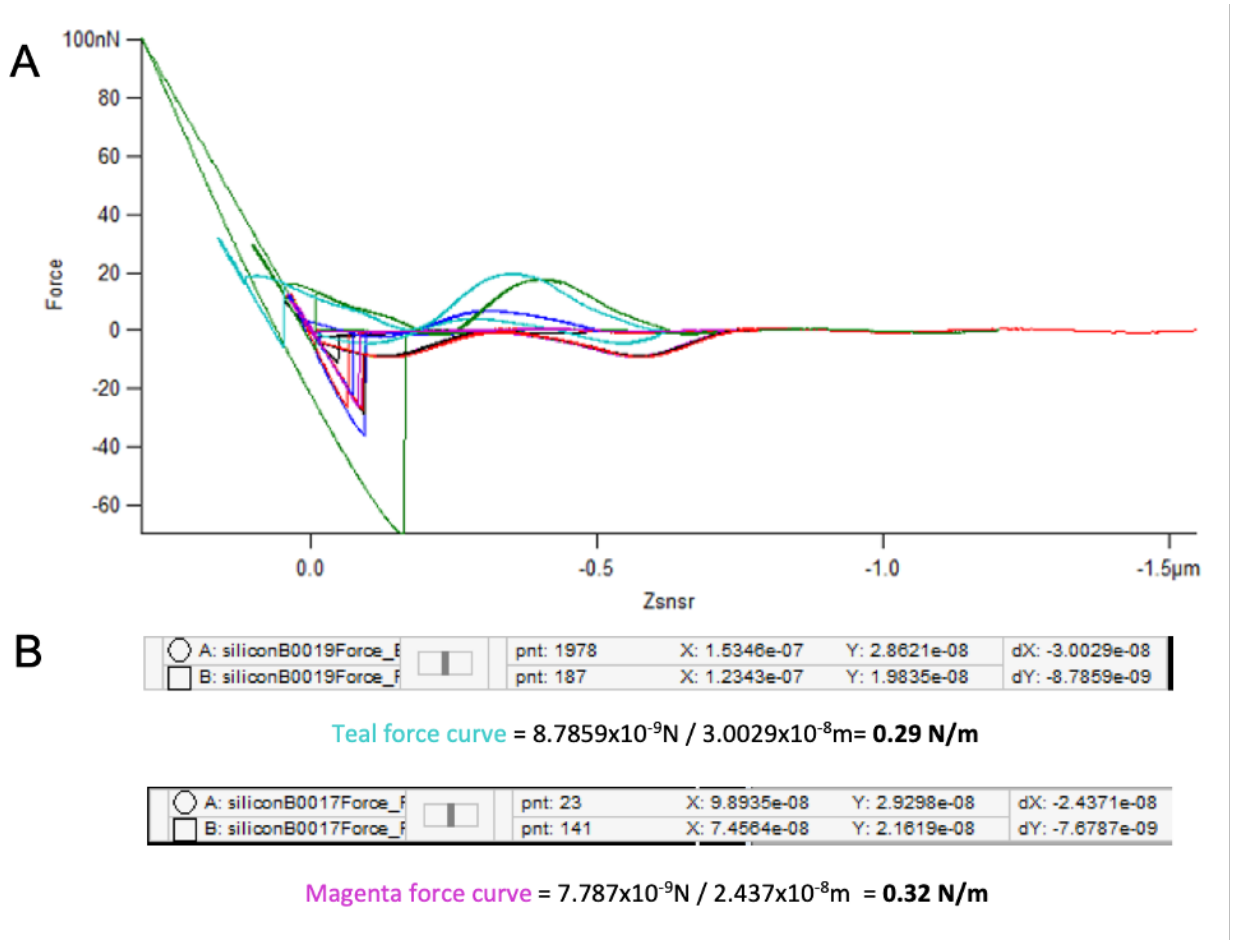

Figure 3.5: (A) 30 different force curves were taken on a silicon electrode on a 30 x 30µm image window that included trace, trough, and recording site features. Only 13 force curves were selected to be analyzed in this graph due to completeness and shape of the curve (curves that interacted with debris particles and not the surface were not analyzed in this data set). The resulting bending stiffness from the magenta force curve was calculated as the slope to be 0.32 N/m and the teal force curve was calculated to be 0.29 N/m. (B) A snap shot in IGOR 6.37 using crosshairs to select arbitrary points on the slope to calculate bending stiffness.

researchers could investigate to understand its direct impact to chronic device performance? Are there biomarkers that are only expressed when cells are optimally attached at the tissue interface? If multiple features affect how cells attach to their surface and researchers are suggesting ranges to which cellular adhesion is best, there are extrinsic properties of the surface environment that affect cell signaling and indirectly, the cell population's transcriptome. Given the evidence of change in differential expression of naïve tissue and tissue at the probe interface (Thompson et al. (2021)), in conjunction with optimal roughness conditions reported with cellular adhesion (Ereifej et al. (2011, 2018a); Stiller et al. (2018)), this gives us rationale to explore a tissue model that can (A) mimic in vivo genetic change, and (B) respond to implantable probe surfaces to further predict device performance.

In chapter four, we will explore a reactive astrocyte culture model to validate its transcriptome with that of rat tissue, in hopes of using a model that could be analyzed through multi-modal high put screening to elucidate possible biomarkers of interest for researchers to investigate FBR.

CHAPTER 4

GENE EXPRESSION CHANGES IN CULTURED REACTIVE RAT ASTROCYTE MODELS AND COMPARISON TO DEVICE ASSOCIATED EFFECTS IN THE BRAIN

4.1 Introduction

Lost neuronal function can be partially returned in tetraplegic patients with implanted microelectrode arrays (MEAs), as demonstrated in clinical trials (Hochberg et al. (2006, 2012); Kim et al. (2008); Simeral (2011)). This technology has helped these patients to communicate with external assistive devices to regain independence in their daily living. Likewise, these devices have the potential to treat epileptic, Alzheimer's, Parkinson's disease, multiple sclerosis patients, and patients suffering from addiction. Although the impact of this technology is profound, an ongoing challenge in this field is presented by the instability and limited longevity of recorded signals detected by implantable electrodes. Researchers in this field have long suspected that the foreign body response (FBR) to the implant contributes to the eventual loss of probe signal (Barrese et al. (2013); Biran et al. (2005); Kozai et al. (2015a)), and have responded by creating a myriad of next generation probes (Thompson et al. (2019)) to mitigate, increasing the design space, however each design comes with its limitations (Thompson et al. (2019)). Understanding the biological response to electrodes may offer an avenue to improve chronic performance and amplify the already-compelling therapeutic promise of these devices.

The stereotypical pathophysiologic response to MEAs occurs in the following stages: (1) device insertion typically causes mechanical damage to tissue, breach of the blood-brain barrier (BBB) and disruption of vasculature at the implantation site; (2) microglia are activated to encapsulate the probe immediately thereafter, creating a physical barrier responsible for limiting ionic exchange with the probe while potentially releasing inflammatory cytokines (Kozai et al. (2015a)); and (3) reactive astrocytes form an encapsulating sheath around the electrodes in the following weeks, increasing impedance as neuronal loss ensues within the recordable radius of the injury site (Kozai et al. (2015a)). This last phase, in which astrocyte function plays a complex role in the immune

response and device performance, remains poorly understood: how does reactive gliosis contribute to suboptimal performance? Is it merely a barrier to signal transmission and a source of increased impedance, or does it influence the function of local neurons (Salatino et al. (2018))? Recent literature suggests that reactive astrocytes are highly heterogeneous, and may have either beneficial or detrimental effects on the healing of central nervous system damage (Liddelow & Barres (2017)). These effects are injury dependent, meaning their expression is determined by the detected change in brain microenvironment following insult. Ischemia tends to lead to the activation of signal transducer and activator of transcription 3 (STAT3), which induces a neuroprotective state and releases those factors, while mechanical damage tends to lead to the activation of nuclear factor kappa B (NF-kB), which releases neurotoxic factors (Li et al. (2019)). Neurotoxic reactive astrocytes may kill the healthy neurons, and furthermore, these astrocytes are associated with a loss in ability to maintain and support synapses (Liddelow & Barres (2017)).

We hypothesized that reactive astrocytes may contribute to the neuronal loss and reduction in dendritic spine densities that have been observed surrounding implanted electrodes (Biran et al. (2005); Gregory et al. (2021)) potentially contributing to decreased chronic signal-to-noise ratio (SNR) for implanted electrodes. Reactive astrocytes deviate from normal gene expression and function of brain homeostasis, and specific patterns of gene expression have been associated with neurotoxic or neuroprotective astrocytic phenotypes (Li et al. (2019)). Changes in gene expression have been noted surrounding devices in recent literature by identifying differentially expressed (DE) genes of astroglial scarring post explantation (Bedell et al. (2020)); these DE genes include many of the biomarkers associated with neurotoxic astrocytes induced by inflammation (Bedell et al. (2020); Thompson et al. (2021)). Our lab's recent work has expanded on this body of knowledge by comparing the change in genetic expression of implanted and naïve tissue at varying distances away from the injury site, for different timepoints (Thompson et al. (2021)). However, the analyzed tissue includes an amalgam of cell types, and the transcriptional profile of reactive astrocytes surrounding devices remains unclear.

We sought to investigate the relationship between gene expression in glial fibrillary acidic

protein (GFAP)-expressing tissue surrounding silicon arrays explanted arrays (Bedell et al. (2020); Ereifej et al. (2018a); Thompson et al. (2021)), and biomarkers of reactive astrocytes (Liddelow & Barres (2017)). To do this, we explored the similarity between cultured reactive astrocyte models and the transcriptional profiles associated with astroglial scarring surrounding implanted electrodes in the rat brain, as revealed via combined immunohistochemistry and spatial transcriptomics. We investigated two reactivity models: rat cortical astrocytes exposed to either microglial-derived cytokines (Liddelow & Barres (2017)), or lipopolysaccharide (LPS, a more generalized reactivity model that induces an infection-like response (Cheli et al. (2017)). We found that the astrocytes surrounding devices bore a more similar expression pattern to cytokine-induced astrocytes than LPS-exposed cells. By investigating the expression pattern between device-associated astrocytes and cultured models, we revealed novel genes associated with the astrocytic response surrounding devices, including genes associated with lipid metabolism and neurodegeneration. These results revealed new insight into the phenotype of device-reactive astrocytes, as well as the utility of in vitro models to explore reactivity *in vivo*.

4.2 Methods

4.2.1 Cell Culture

Our cytokine-induced cell culture model is inspired by the reactive astrocyte model that was used in the *Liddelow et al.,* 2017 publication (Liddelow & Barres (2017)), which was derived from methods developed by *Foo et al., 2011* (Foo et al. (2011)). In the Foo and Liddelow methods, they subjected their postnatal astrocytes to several rounds of immunopanning to purify their cultures. To simplify our approach, and considering the heterogeneity expected in vivo, we did not immunopan our cultures. Additionally, since these are fetal rodent astrocyte cells, we passaged them for a total of 4 times, with a 1 to 3 split each time, as literature suggests that glial culture does not have the characteristics of mature glia until they have been in culture for roughly 35 days (Gilmour et al. (2019)).

For our study, E-18 fetal rat cortical astrocytes (Gibco, $4x10^6$) were seeded in a 6-well plate

at a cell density of 200,000/cm2 in Dulbecco's Modified Eagle Media (DMEM, Thermo Fisher) supplemented with 15% fetal bovine serum (Gibco) for a total number of four passages. As discussed previously (Gilmour et al. (2019)), astrocyte maturity is an important consideration when inducing a reactive state. Our pilot experiments using qPCR indicated that C3, a biomarker for cytokine-induced reactivity, was induced most reliably following four passages in vitro (4 weeks in culture, data not shown). Cells were then transferred into serum-free media for a period of six days prior to treatment with a cytokine cocktail or LPS. As such, the entire culture period is comparable to the 35 day time frame recommended to achieve adequate glial maturity (Gilmour et al., 2019). More specifically, on the fourth passage, astrocytes were transferred to 24-well plates and treated with a serum-free media containing 50% neurobasal, 50% DMEM, 292 µg/mL L-glutamine, 1mM sodium pyruvate, 5µg/mL N-acetyl cysteine, 100 U/mL penicillin, and 100 µg/mL streptomycin, as described by previous protocols (Liddelow et al., 2017). Every 3 days, the cells were supplemented with 5 ng/mL HBEGF (Peprotech, 100-47), for a total incubation time of 6 days in vitro, and then treated for 24 h with C1q (30 ng/mL, MyBioSource, MBS143105), IL-1α (3 ng/mL, Sigma I3901) and TNF (30 ng/mL, Cell Signaling Technology, 8902SF), based on reported methods (Liddelow & Barres (2017)). As a positive control, separate serum free E-19 astrocytes were treated with lipopolysaccharide (LPS, O55:B5, Sigma Aldrich, 1µg/mL) for 24 h based on reported methods. Following the 24 hour period, media was removed and cultures were thoroughly rinsed with PBS. After the buffer was completely aspirated, plates were stored at -80C until RNA extraction.

4.2.2 RNA Extraction and Sequencing

Total RNA was extracted from cultured reactive astrocytes using RNAzol (Molecular Research Center, Inc) and RNEasy (Qiagen) extraction kits. The samples were then submitted to the University of Michigan Advanced Genomics core for library preparation and sequencing. Samples were subjected to 150 base paired end cycles on the NovaSeq-6000 platform (Illumina). Differential expression analysis was performed by the University of Michigan Bioinformatics Core. Data were

first pre-filtered to remove genes with 0 counts in all samples. Differential gene expression analysis was performed using DESeq2 (Love et al., 2014), using a negative binomial generalized linear model (thresholds: linear fold change >1.5 or <-1.5, Benjamini-Hochberg FDR (Padj) <0.05). Plots were generated using variations of DESeq2 plotting functions and other packages with R version 3.6.3. Genes were annotated with NCBI Entrez GeneIDs and text descriptions. Functional analysis, including candidate pathways activated or inhibited in comparison(s) and GO-term enrichments (Mi et al., 2019), was performed using iPathway Guide (Advaita) (iPathwayGuide), (Draghici et al., 2007). DE genes in cell culture models were used for additional gene ontology (GO) analysis. The PANTHER Classification System26 was used for this purpose, and significant (p-value < 0.05) and highly enriched GO terms are reported for lists of DE genes expressed unique to each cell culture model, as well as the list of DE genes in both models. Specifically, the PANTHER Overrepresentation Test (Fisher's exact test, Release: February 24, 2021) was used with a Rattus norvegicus reference from the GO Ontology database and GO biological process complete dataset for (DOI: 10.5281/zendo.5228828, Release: August 8, 2021).

4.2.3 Spatial Transcriptomics

Data was gathered using methods previously described (Whitsitt, et al. 2021). Briefly, a 10x Genomics (Pleasanton, CA) spatial gene expression platform ("Visium") was used to assess brain tissue sections from Sprague-Dawley rats implanted with a silicon Michigan-style electrode (A1x16-3mm-100-703-CMLP, 15 um thickness, NeuroNexus Inc, Ann Arbor, MI) for either 24 hours, 1 week, or 6 weeks. Each spot with spatially resolved gene expression in figures 11-13 is 55µm in diameter and 100µm apart, center-to-center. Prior to sequencing, tissue sections were labeled using immunohistochemical methods for neuronal nuclei (rabbit anti-NeuN, 1:100, Abcam, cat. : 104225) and glial fibrillary acidic protein (mouse anti-GFAP, 1:400, Sigma-Aldrich, cat. : G3893), and cell nuclei were counterstained using Hoechst (10 µg/mL). Images were collected as previously described (Whitsitt 2021). Using the LoupeBrowser software interface (10X Genomics), differential gene expression analysis compared the gene expression of the cluster of spots within

150μm of the device interface to the cluster of spots greater than 500μm from the device interface, excluding the spots under the glia limitans. This yielded 31 differentially-expressed (DE) genes at 24 hours, 1137 DE genes at 1 week, and 164 DE genes at 6 weeks ($p<0.05$).

4.2.4 Comparison of RNA Sequencing of Cultured Reactive Astrocytes to Spatial Transcriptomics

DE genes from each timepoint in vivo were compared to DE genes from the in vitro cytokine and LPS-treated astrocyte models. Genes were selected for further investigation if they appeared in both the in vivo and in vitro experiments and their LFC had the same sign (positive or negative). Lists of genes meeting these criteria were made for each in vivo timepoint for both the cytokine and LPS in vitro conditions (24 hours/cytokine, 24 hours/LPS, 1 week/cytokine, 1 week/LPS, 6 weeks/cytokine, 6 weeks/LPS).

4.3 Results and Discussion

We detected 927 differentially expressed genes between cytokine-treated cells and controls, 1,183 DE genes between LPS-treated cells and controls, and 831 genes between cytokine- and LPS-treated cells (volcano plots shown in **figure 4.1**). We noted that certain genes were significantly upregulated in both models ("pan-reactive" genes) and others were specifically upregulated only in cytokine-induced or LPS-treated cells ("unique" genes). Of the significantly DE genes, 311 were shared between the two models (**figure 4.2**), yielding 616 unique cytokine-induced genes and 872 unique LPS-treated genes. While we highlight specific genes for further discussion in the following sections, complete differential expression results, as well as spatial transcriptomics data, are supplied as supplementary files. We focus our discussion on the unique genes to each model, and compare results with *in vivo* responses.

4.3.1 Unique Cytokine - Induced Genes

As expected, cytokine treatment induced upregulation of complement-associated genes. The complement cascade is involved in the innate immune response and includes an important class

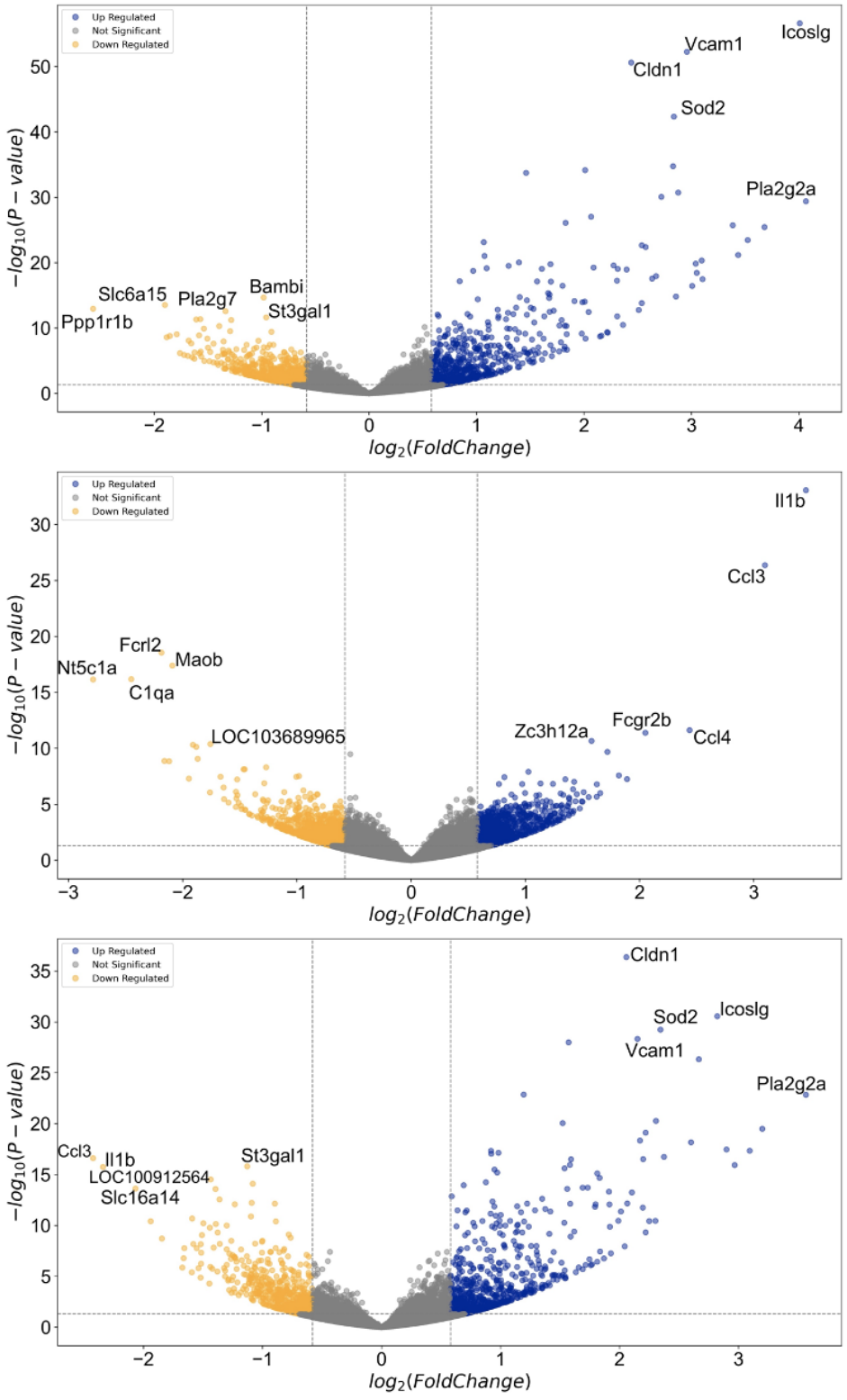

Figure 4.1: Volcano plots of LPS and cytokine-induced reactive astrocyte models. Both cytokine treatment and LPS exposure induced hundreds of significantly DE genes in comparison to control cells. Significance was determined as a Log2FoldChange > 0.6, and p<0.05

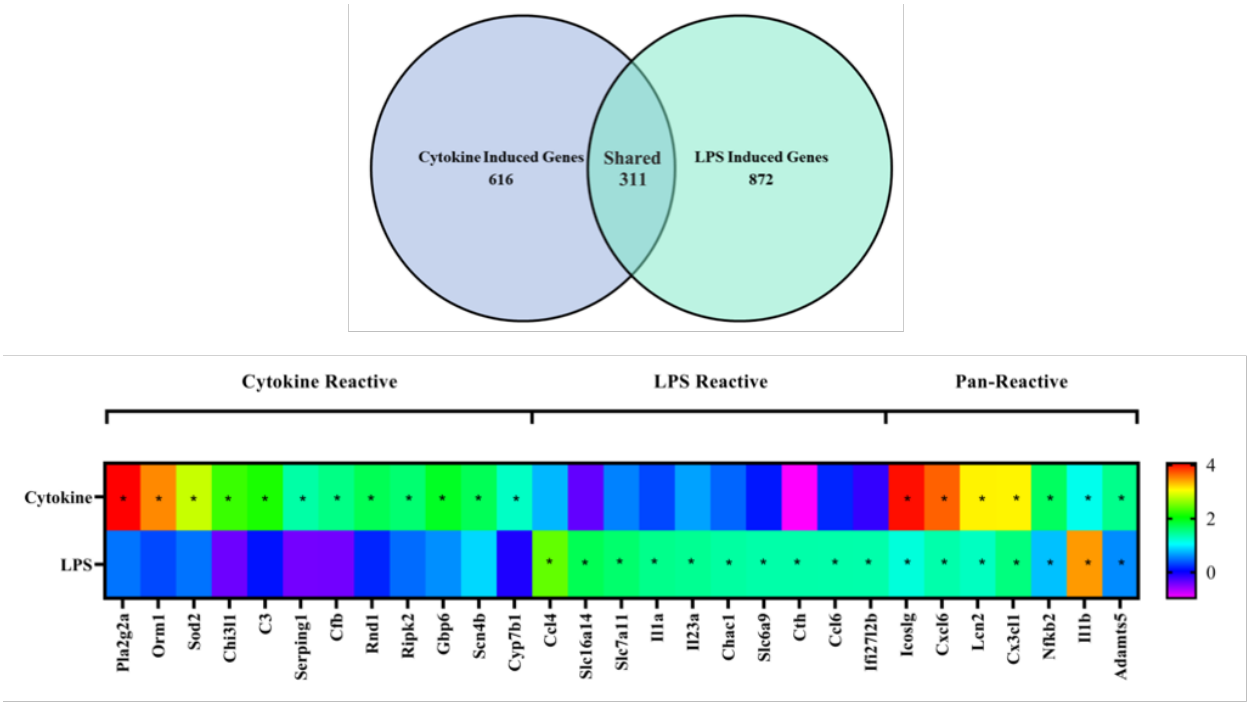

Figure 4.2: Comparison of LPS and cytokine-induced reactive astrocyte models. Both cytokine treatment and LPS exposure induced hundreds of significantly DE genes in comparison to control cells, where 311 genes were shared between the two models (Venn diagram at left). Examples of individual genes which were significantly differentially expressed in each condition as well as those which were shared ("pan-reactive") (heatmap below). Color bar shows the Log2FoldChange versus control cells, and "*" denotes statistical significance ($p<0.05$).

of genes upregulated in both neurodegenerative diseases (Liddelow & Barres (2017); Liddelow et al. (2017); Li et al. (2019)) and traumatic brain injury (TBI) (Wei et al. (2020)). Complement component 3 (C3), which was identified as a key biomarker of cytokine-induced astrocytes in the seminal report by *Liddelow et al.* (Liddelow & Barres (2017)), was significantly and specifically upregulated in cytokine-treated cells in our data (**figure 4.1**). Likewise, complement factor B (Cfb) upregulation was unique to our cytokine-induced culture model. Cfb encodes an astrocyte-derived factor that supports survival of microglia (Presumey et al. (2017)), which promote synaptic pruning in the phagocytic reactive state. Given our observations of a reduction in synapses surrounding implants, as well as the observation of increased C3 at the device interface (Thompson et al. (2021)), the upregulation of complement genes is an aspect of the cytokine-induced astrocyte model which resembles *in vivo* effects.

We also noted the increased expression of many interesting enzymes associated with the reactive phenotype conversion in cytokine-induced cells. Phospholipase A2 (*Pla2g2a*) registered the highest fold change of any gene, and it was uniquely DE in the cytokine condition. Phospholipase A2 is an enzyme that hydrolyses phosphoglycerides to yields fatty acids and leads to the production of eicosanoids (Stephenson et al. (1999)). *Pla2g2a* was found to be expressed in reactive astroglia only in the areas where neuronal death occurred (Guttenplan et al. (2021); Stephenson et al. (1999)). Other enzymes detected in our data are associated with the transition to a reactive phenotype, which occurs when astrocytes sense and react to exogenous agonists (Agulhon et al. (2013); Porter & Mccarthy (1995a,b)) and neurotransmitters released from presynaptic clefts (Agulhon et al. (2013); Kang et al. (1998); Perea & Araque (2005)). Astrocytic end-feet express g-coupled proteins that become phosphorylated by rho GTPase 1, which is the enzyme that becomes activated when activating microenvironment changes occur. We observed increased expression of Rho family GTPase 1 (Rnd1) specifically in the cytokine-induced astrocytes. Phosphorylation of g-coupled proteins in astrocytes encourages calcium channel expression, (Agulhon et al. (2013)) which we have observed using immunohistochemistry in this culture model (not shown); literature suggests an upregulation in calcium channel expression during the conversion of normal to reactive astrocyte (Barres et al. (1989); Cheli et al. (2017)). Another upregulated enzyme, Receptor Interacting Serine/Threonine Kinase 2 (RIPk2), contains a C-terminal caspase activation and recruitment domain (CARD) and is a component of signaling complexes in both the innate and adaptive immune pathways (Ferreira et al. (2019)). It is a upstream regulator and potent activator of NF-kappaB and is an inducer of apoptosis in response to various stimuli (Ferreira et al. (2019)). NF-kappaB activation is required for neurotoxic reactive astrocyte expression (Li et al. (2019)). A downstream biomarker, superoxide dismutase 2 (Sod2), is a free radical scavenging enzyme which is expressed in Alzheimer's Disease, aging, ischemic stroke, and Parkinson's Disease (Flynn & Melov (2013)). Interestingly, it also has been identified in explanted rat tissue surrounding the injury site of microelectrode array shanks (Ereifej et al. (2018a)).

We also observed an upregulation of the expression of several genes associated with ion

channel expression and activation. Guanylate binding protein family member 6 (Gbp6) is a protein, induced by interferon, which hydrolyzes guanine triphosphate (GTP) to guanine diphosphate (GDP) and guanine monophosphate (GMP). It is catalyzed by rho GTPase and plays a role in calcium channel activation in astrocytes. Another detected gene, sodium voltage-gated channel beta subunit 4 (Scn4b), activates $Na_v1.5$ in the wake of mechanical damage. Scn4b is specifically linked to $[Ca^{2+}]$i gradient shifts and promotes glial scarring (Pappalardo et al. (2014)). Changes in ion channel expression have been observed surrounding devices in our previous data, when Na_v expression developed an inverse relationship with K_v expression when developing from acute to chronic injury (Salatino et al. (2019)).

4.3.2 Unique LPS-induced genes

LPS activates the Toll-like receptor 4 (TLR4)-dependent pathway that induces microglia to release IL-1β, IL-6 and TNFα via the mitogen-activated protein kinase (MAPK) and NFkB pathways (Noailles et al., 2018). As expected, IL-1β and IL-23α were observed as uniquely upregulated in our LPS-treated cells. There was a lesser association of this model with complement-associated genes, which is not unexpected because the complement component system is activated by pathogens, whereas LPS is an endotoxin. True to what is observed in reactive astrocyte transcriptomes, we also observed the upregulation of chemokine genes in LPS-treated cells. This included the upregulation of inflammation-associated factors such as C-C motif chemokine ligand 3 (Ccl3), which is induced typically through the STAT3 pathway, and is reduced through nicotinamide adenine dinucleotide phosphate oxidase (NOX2) inhibition (Chen et al. (2011)). *Chen et al.'s* studies suggest that NOX2 inhibition may provide neuroprotection against inflammatory damage (Chen et al. (2011)). In addition, C-C motif chemokine ligand 4 (Ccl4) is upregulated in the LPS condition and has been associated with neurodegenerative diseases including Alzheimer's disease and HIV-associated dementia (Zhu et al. (2015)). Finally, c-c motif chemokine ligand 6 (Ccl6) was upregulated in LPS-treated cells. Ccl6 has been associated with mediation of astroglial migration (Kanno et al. (2005)). Its expression in chronic reactive astrocytic populations surrounding

explants provides evidence of reactive astrocytic migration (Kanno et al. (2005); Zamanian et al. (2012)). All three of these chemokines (Ccl3, Ccl4, Ccl6), which were selectively upregulated in our LPS-treated astrocyte cultures, are associated with oxidative stress-induced brain injury (Chen et al. (2011); Ereifej et al. (2018a); Kanno et al. (2005); Zhu et al. (2015)).

Endotoxins can cause apoptosis, and we observed enzymatic biomarkers that are key regulators of apoptotic pathways. Glutathione Specific Gamma-Glutamylcyclotransferase 1 (Chac1) has been shown to promote neuronal differentiation by deglycination of the notch receptor, ultimately inhibiting neurogenesis (Chen et al. (2011)). This enzyme depletes glutathione, which is a necessary factor in the apoptotic cascade (Chen et al. (2011)). Solute carrier family 6 member 9 (Slc6a9) plays a role in shuttling glycine during deglycination and has been found to be upregulated in patients with other neurodegenerative diseases associated with erythrocyte dysregulation, such as cerebral malaria (Cabantous et al. (2020)). Additionally, there are alternate pathways to arrive to apoptosis. A common way to tag proteins for cell death is through methylation. Cystathionine gamma-lyase, (Cth), which is upregulated in our data, does this by converting cystathionine to cysteine, which also increases the elevation of total homocyesteine (tHcy), a risk factor expressed in Alzheimer's disease and cognitive loss (Roman et al. (2019)).

The consistent, significant upregulation of particular biomarkers observed across several disease states can potentially suggest specific characteristics of astrogliosis (Merienne et al. (2019)). Interferon, alpha-inducible protein 27 like 2B (Ifi27l2b), that participates in apoptotic signaling, has been observed in our LPS dataset but also in Merienne et al.'s work performing transcriptome profiles of astrocytes, microglia, and spiny neuron projections of the striatonigral and striatopallidal loops (Merienne et al. (2019)) and in *Zamanian et al.'s* reactive astrocyte transcriptome data (Zamanian et al. (2012)). Another biomarker observed in our LPS data set which is associated with disease states, such as Alzheimer's disease and cognitive loss, is solute carrier family 16, member 14 (Slc16a14). Slc16a14 codes for monocarboxylic acid transporters, which are highly expressed in the hippocampus and hypothalamus (Roshanbin et al. (2016)). Likewise, solute carrier family 7 member 11 (Slc7a11), is highly expressed in glioma patients and may be responsible for seizures

(Robert et al. (2015)); it is upregulated in microenvironments experiencing neurotoxic levels of glutamate (Robert et al. (2015)).

4.3.3 Gene Ontology for Cytokine, LPS, and Pan-reactive Genes

In addition to "unique" genes associated with each model, we also observed several genes that are associated with both models ("pan-reactive" genes), which are likely indicative of a generalized reaction to stimulation. We also observed upregulation of genes in our models that are associated with "normal" physiological function. For example, ADAM metallopeptidase with thrombospondin type 1 motif, 5 (Adamts5) was upregulated in both culture models in comparison to controls, which is enables extracellular matrix (ECM) and heparin binding (Coronel et al. (2019)). The differential expression of genes associated with normal homeostatic pathways co-existing with differential expression of inflammation-associated genes in our reactive models aligns with the theory that reactive astrocyte populations exist on a continuum of phenotypes (Liddelow & Barres (2017)).

4.3.4 Comparisons of Gene Induction in Cell Culture Models to the In Vivo Tissue Response

To contextualize the cellular origin of recently observed changes in gene expression surrounding electrodes, we sought to compare gene expression in cultured astrocyte models to gene expression surrounding devices implanted in the brain. To do this, DE genes from each timepoint in vivo were compared to DE genes from the in vitro cytokine and LPS-treated astrocyte models. Genes were selected for further investigation if they appeared in both the in vivo and in vitro experiments and their LFC had the same sign (positive or negative). Lists of genes meeting these criteria were made for each in vivo timepoint for both the cytokine and LPS in vitro conditions (24 hours/cytokine, 24 hours/LPS, 1 week/cytokine, 1 week/LPS, 6 weeks/cytokine, 6 weeks/LPS). Cytokine and LPS intersections with the 24 hour in vivo DE genes each yielded 256 and 260 genes. The Cytokine and LPS intersections with 1 week in vivo DE genes yielded 104 and 66 genes. The Cytokine and LPS intersections with 6 week in vivo DE genes yielded 38 and 21 genes, respectively. Further analysis separated pan-reactive genes (those common to all models) from genes unique to each reactivity

model to determine which reactive astrocyte model, Cytokine or LPS, is most aligned with in vivo observations. After pan-reactive genes were removed from the in vivo vs. cytokine intersections, there were 165 unique genes found at 24 hours, 71 genes found at 1 week, and 23 genes found at 6 weeks. After pan-reactive genes were removed from the in vivo vs. LPS intersections, there were 169 unique genes found at 24 hours, 33 genes found at 1 week, and 6 genes found at 6 weeks. The composite expression patterns of these genes, at each time point, are shown in **figures 4.3 and 4.4**.

We further explored the spatial patterns of the expression of individual cytokine-induced genes surrounding the device tracts at each time point. Examples of individual genes at each time point are displayed in **figure 4.5**. These genes were selected for display based on a combination of high differential expression in the cytokine-induced culture model, localized expression associated with the electrode implant, and relevancy to reactive astrocytes based on reported literature. The cytokine-induced genes included significant differential expression of both complement component 3 (C3) and Serping1, as reported previously (Liddelow & Barres (2017)). Upon inspection of the electrode interface, we observed tight clustering of the expression of these genes in the compact GFAP-expressing scar surrounding the device tract **figure 4.5**. As a complement-associated protein, astrocytic C3 expression is associated with the neuroinflammatory response in neurological injuries and diseases, as well as with the loss of synaptic connectivity between neurons (Liddelow & Barres (2017)). Our recent work reported elevated C3 expression within 100 microns of the electrode interface (Thompson et al. (2021)), and the present study revealed overlap of C3 expression with the presence of GFAP-positive astrocytes surrounding the electrode. The expression of these genes in astrocytes encapsulating the device suggests a potential relationship of these cells with synaptic loss surrounding devices.

In addition to these effects, which were forecast by previous transcriptomic profiling in cytokine-induced astrocytes, we observed new markers of device-reactive astrocytes through our comparative investigation. For example, 24 hours post electrode implantation, Junb was found to be upregulated compared to a non-implanted tissue section. At the 1 week time point, cytochrome P450 family

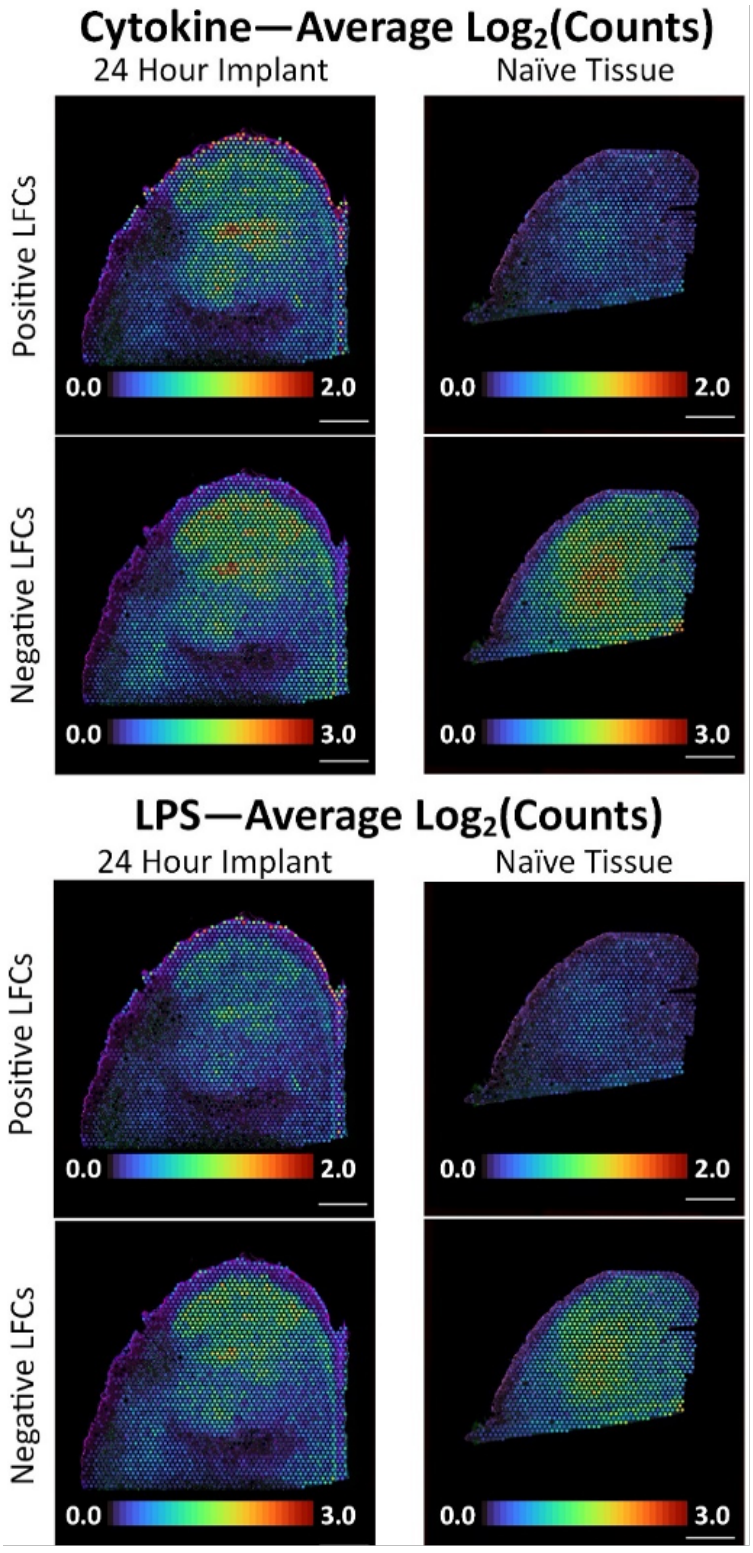

Figure 4.3: Average expression of genes differentially expressed both in astrocytes in vitro and in a 24-hour electrode implant in vivo. Cytokine panels show the average number of counts for the genes that were found to be differentially expressed in both the cytokine treated astrocyte cultures and in a 24-hour electrode implant in vivo compared to a naïve, non-implanted tissue section. LPS panels show this same data except for genes differentially expressed in the LPS treated astrocytes and the 24-hour implant. Scale bars: 1000 µm.

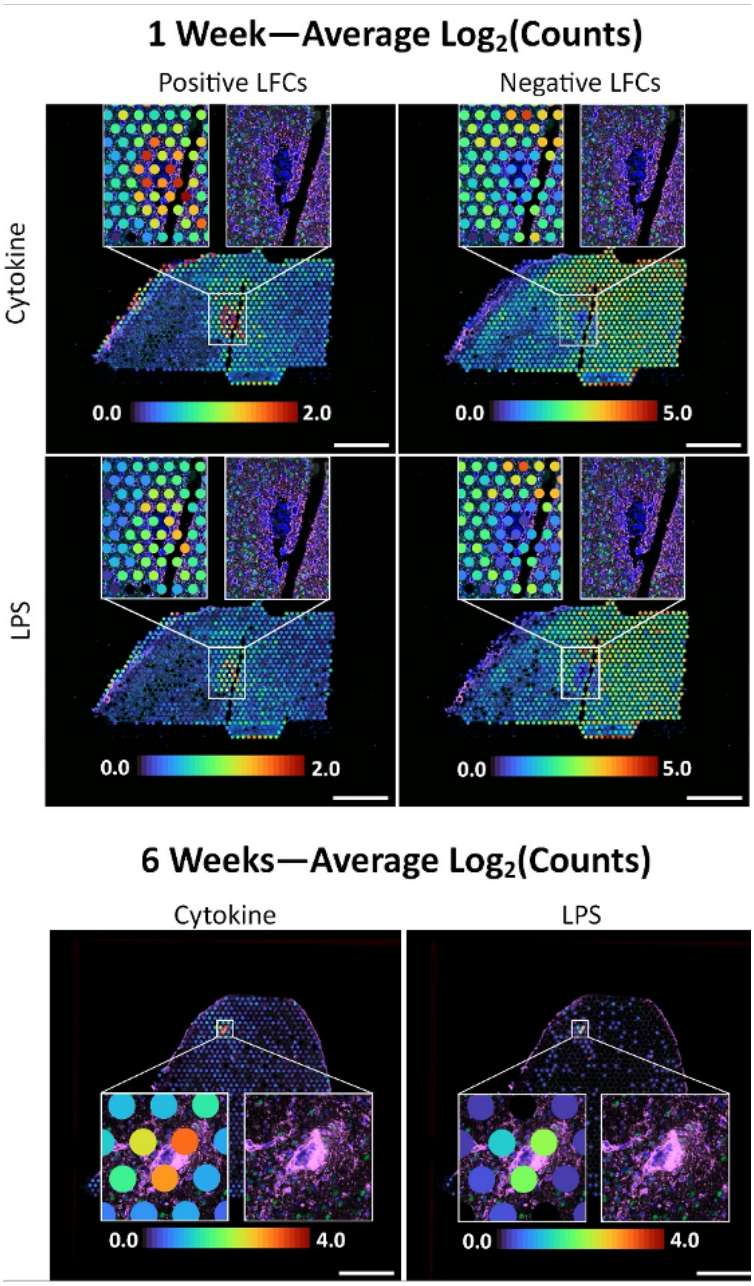

Figure 4.4: Average expression of genes differentially expressed both in astrocytes in vitro and in 1-6-week electrode implants in vivo. Cytokine panels show the average number of counts for the genes that were found to be differentially expressed in both the cytokine treated astrocyte cultures and in in vivo tissue sections. LPS panels show this same data except for genes differentially expressed in the LPS treated astrocytes and the 1-and 6-week implants. The 6-week in vivo experiment yielded no negative differentially expressed genes, thus these samples have no "Negative LFC" genes. Scale bars: 1000 µm.

7 subfamily B member 1 (Cyp7b1) was noted. Cyp7b1 is an enzyme needed for the synthesis of an oxysterol implicated in astrocyte migration (Rutkowska et al. (2015)). Chitinase 3-like protein 1 (Chi3l1) was revealed in astrocytes at the device interface at the 6 week time point. Chi3l1 encodes a secreted glycoprotein (YKL-40) which has been associated with reactive astrocytes and neurodegeneration in several reports (Lananna et al. (2020); Matute-Blanch et al. (2020)). Its expression is known to increase in parallel with tau in Alzheimer's disease (AD), and a recent investigation in a mouse model of AD suggested that, "Chi3l1 may suppress glial phagocytic activation and promote amyloid accumulation (Lananna et al. (2020))." It is possible that its presence at the 6 week time point surrounding electrodes could serve to dampen and constrain glial reactivity as the device interface stabilizes. Since tau pathology has been observed at chronic time points (16 weeks) surrounding implanted electrodes, it is likewise possible that Chi3l1 contributes to emergence of AD-associated markers surrounding implants (Mcconnell et al. (2009)). Future work will need to be conducted to explore the relationship between Cyp7b1 expression and the formation of an astroglial sheath, as well as a subsequent, potentially multi-faceted role for Chi3l1 in constraining glial responses at the expense of neuronal health. These are two examples of genes revealed through our analysis; raw data files and analysis results are available for further investigation (Tables, loupe browser files, etc).

4.3.5 Discussion of Relevancy of Culture Models

An *in vitro* testbed would be valuable to test hypotheses and develop approaches to screen designs and intervention strategies in a high throughput manner, and gene expression is a potentially useful readout to enable the development of such an assay. Previous studies have sought to identify culture conditions which model the foreign body response to electrodes implanted in the brain. An early iteration of this approach employed a 'scrape' injury, or the placement of a segment of wire, within a co-culture of microglia, astrocyte, and neurons (Polikov et al. (2005)). Observations of glial migration and device encapsulation recreated familiar elements of device-tissue interaction. Several subsequent reports iterated on this approach, with improvements including the addition

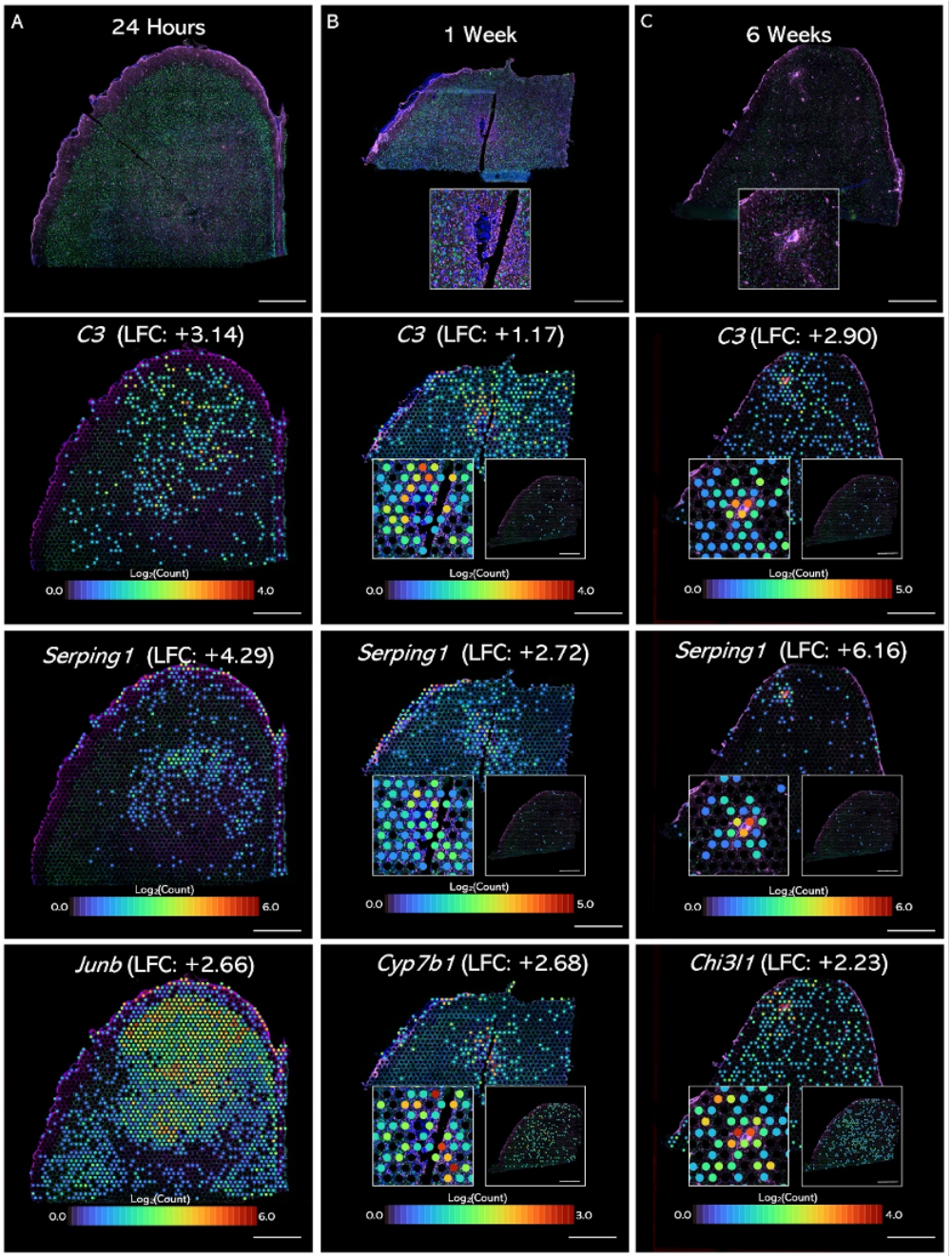

Figure 4.5: Individual expression of cytokine genes of interest in each of the in vivo tissue sections. (A) IHC image of the 24-hour implant tissue section. Below, C3, Serping1, and Junb expression (Log2(Counts)) in the 24-hour section is shown. (B) IHC image of the 1-week implant tissue section. Below, C3, Serping1, and Cyp7b1 expression in the 1-week tissue section is shown. Call out images show a zoomed image of gene expression around the electrode tract on the left, and the expression of each gene in a naïve tissue section on the right. (C) IHC image of the 6-week implant tissue section. Below, C3, Serping1, and Chi3l1 expression in the 6-week tissue section is shown. Call out images show a zoomed image of gene expression around the electrode tract on the left and the expression of each gene in a naïve tissue section on the right. IHC images (Green: NeuN, Magenta: GFAP, and Blue: Hoechst). Scale bars: 1000 µm.

of oligodendrocytes (Gilmour et al. (2019)), the inclusion of inflammatory mediators such as lipopolysaccharide (Polikov et al. (2006)), and the development new culture protocols to reduce the experimental burden associated with long, continuous cultures (Gilmour et al. (2019)).

Our approach focused specifically on astrocyte reactivity as a potential pathway of interest, with the goal of informing our recent observations of device-induced gene expression using spatial transcriptomics (Thompson et al. (2021)). Our methods were derived from studies using LPS to induce inflammation in astrocytes (Cheli et al. (2017)), as well as a more recently reported, cytokine-induced astrocyte model (Liddelow & Barres (2017)). The latter approach is of particular interest, as the microglial source of cytokine release, as well as reported effects on synaptic connectivity, are reminiscent of the brain tissue response to electrodes. While each culture model expressed genes relevant to inflammatory responses at the device interface, our initial inspection indicated a closer correspondence of the cytokine-induced model with the in vivo tissue response (**figure 4.3**). Additionally, the approach revealed new genetic markers overlapping with glia at the device interface (e.g., Chi3l1) (**figure 4.4**). Nonetheless, limitations remain in our current study: our simplified culture method in comparison to the original report may have increased astrocytic heterogeneity, and questions remain regarding the similarity of these models to responses in the intact brain. Future analysis using more advanced computational techniques may elucidate biomarkers more effectively, and armed with an increasing knowledge base of the relationship between devices and gene expression (Bedell et al. (2020); Stieglitz (2001)), it may be possible to further refine the culture models used to more faithfully recreate these responses in future work.

4.3.6 Clinical Relevancy and Future Directions

Rodent models are the gold standard *in vivo* model used to study response to probes, followed by tissue culture inflammatory models. However, compared to the intact human brain, mouse models have less diverse astroglial populations, limiting the ability to accurately predict human patient outcomes (Fomchenko & Holland (2006)). Also, because of a short life cycle, murine models are not reliable indicators of potential long-term performance in human patients. Additionally,

2-dimensional culture models suppress important genetic expression (Li et al. (2012a)) because they do not actively mimic the biochemical and mechanical properties of the 3-dimensional brain microenvironment. The dynamic organelle that houses the brain microenvironment, the extracellular matrix (ECM), consists of proteoglycans and glycosamioglycans such as hyaluronic acid, meaning the mechanical properties of the functional tissue are governed by these macromolecules (Quail & Joyce (2017)). Astroglial cells have mechanosensing abilities, and placing these cells in a dish result in the diminishment of important brain homeostatic cell signaling.

Emerging techniques using human induced pluripotent stem cell (iPSC)-derived, 3-dimensional brain organoids (Dosso et al., 2020; Lancaster and Knoblich, 2014) may address many of the murine and 2D culture limitations. Spatial and organizational support is needed for self-assembly to support constant rearrangement and cell separation, observed in early cell developmental biology that creates a structurally robust ECM. This encourages the creation of microglia and vascular cells responsible for cell-to-cell communication and immune response. Patterned protocols mimic specific areas of the brain while integrated protocols make whole brain organoids (Dosso et al., 2020), to produce vasculature and immune type cells through coculturing methods (Cakir et al. (2019); Ham et al. (2020); Pham et al. (2018); Wörsdörfer et al. (2019)). In the future, human iPSC brain organoids may be an interesting model to study DE genes surrounding electrodes implanted in the brain. The growing use of transcriptomics in the study of device-tissue interaction already have opened up new understanding of the biological mechanisms of the tissue response to implanted electrodes, paving the way for the future extension of these methods to clinically relevant models of human disease.

In chapter 5, I will expand on this body work concerning future directions.

CHAPTER 5

FUTURE DIRECTIONS

My research goal is to uncover mechanisms that activate pathways of the tissue response at the tissue-electrode interface. Quantitative IHC from my predoctoral lab has observed changes in other voltage gated ion channels sodium (Na_v) and potassium (K_v) expression, for a distance ranging from within 40 microns (at the tissue/electrode interface) to >250μm away from the injury, over a period of 6 weeks. Simultaneously, the expression of vesicular glutamate transporter (VGLUT) has increased expression at the tissue electrode interface at 3 day post-implantation, which became lower than vesicular GABA transporter (VGAT) at the same area by time point 4 weeks out, indicating a shift from hyperexcitability to hypoexcitability (Gregory et al. (2021); Salatino et al. (2019); Thompson et al. (2021)) Similarly, there was an observation of significant differences in plasticity, neuronal firing, and spine density near and 500μm away from the insertion site, (not pictured). We believe that astrocytes sense a change in the mechanical and biochemical environment, initiating a signaling cascade which underlies these results. Further, we believe that these changes cause a shift in normal to a unique, device-reactive phenotype that could serve as an underlying mechanism for our previous observations of shifts in Na_v, K_v, VGLUT and VGAT expression local to devices. As a consequence, and as a function of inflammation, these effects may underlie the initial promotion of, and later protection from, neurotoxicity.

Several additional observations support the role of astrocytes in dictating circuit remodeling. Astrocytes contain a large number of localized G-protein coupled receptors (GqGPCRs) on their processes that allows them to sense and react to exogenous agonists (Agulhon et al. (2013); Porter & Mccarthy (1995a,b)) and neurotransmitters released from presynaptic clefts (Agulhon et al. (2013); Kang et al. (1998); Perea & Araque (2005)). Astrocytes wrap around capillaries, touching neurons; therefore, the presence of GqGPCRs on these processes supports the idea of bidirectional communication between astrocytes and neurons. Furthermore, gliotransmitters (ATP, glutamate, and D-serine) that are released from neurons, cause an increase in the internal calcium level

in astrocytes, which then causes an increase in neuronal ionotropic glutamate receptor (iGluR) activity on neurons from astrocytic-released glutamate (Agulhon et al. (2013)). The discovery of this feedback loop suggests that astrocytes also modulate neuronal activity, supporting the tripartite synapse theory in which pre- and post-synaptic neuron compartments combine with the astrocyte to act as a single functional synapse. Even though there is evidence that supports astrocytic GqGPCR activation by neurotransmitter-based increases in intracellular astrocytic calcium, the exact pathways in which astrocytes release gliotransmitters is unclear. It is possible that the gliotransmitters released by astrocytes act on either the presynaptic or extrasynaptic ionotropic receptors of neurons. Understanding that astrocyte depolarization (Barres et al. (1989)) and mechanical stimulation Wilson et al. (2016)) increases intracellular calcium, I suspect that the signaling pathways stimulated by probe insertion occur very similar to what researchers have observed in alternative studies of astrocyte reactivity and neurodegeneration.

Unfortunately, many of these signaling pathways are diminished in 2D culture because 2D culture models do not actively mimic the biochemical and mechanical properties of the brain, resulting in loss of genetic expression (Li et al. (2012b)). The extracellular matrix (ECM), the structure that houses the biophysical microenvironment of the brain, is made up of brain parenchyma, that consists of proteoglycans, and glycosamioglycans such as hyaluronic acid, meaning the mechanical properties of the functional tissue are governed by these macromolecules (Quail & Joyce (2017)). These building block molecules include those produced by astroglial cells, have mechano-sensing abilities which, are maintained through cell-to-cell communication, and gap junctions (Budday et al. (2017)). In addition, rat models have different populations of astroglial cells that are not as diverse or numerous as human cells, have different pharmacodynamics than humans, and are limited in their ability to predict human patient outcomes (Fomchenko & Holland (2006)). But how can we investigate these signaling pathways more intimately? Can we develop an inflammatory model that is suitable enough to study that can predict patient outcomes?

During my postdoctoral work, I seek to study another physiologically relevant inflammatory model that may be able to produce more clinically relevant outcomes, allowing researchers to an-

swer pertinent questions concerning MEA chronic performance and potentially neurodegenerative pathway signaling. Based on the literature and my predoctoral work, I have hypothesized that astrocytes are responsive to implantation (Michelson et al. (2018)) and probe features, chapter 3, as evidence by shift from hyper- to hypopolarization and morphology near the probe (Salatino et al. (2019)), however my guiding hypothesis in my postdoctoral work, is that a 3D human derived *ex vivo* system can incorporate and mimic, all these factors, enabling the expression of signaling pathways that are more likely to occur in the human brain. The proposed research is expected to illuminate and broaden our understanding of FBR to MEAs.

BIBLIOGRAPHY

BIBLIOGRAPHY

Abaricia, J. O., Farzad, N., Heath, T. J., et al. 2021, Acta Biomaterialia, 133, 58

Abidian, M. R., & Martin, D. C. 2009, Advanced Functional Materials, 19, 573

Agulhon, C., Petravicz, J., Mcmullen, A. B., et al. 2013, Neuron, 59, 932

Ajiboye, A. B., Willett, F. R., Young, D. R., et al. 2017, The Lancet, 389, 1821

Atay, S. M., Kroenke, C. D., Sabet, A., & Bayly, P. V. 2008, Journal of Biomechanical Engineering, 130, 021013

Azemi, E., Lagenaur, C. F., & Cui, X. T. 2011, Biomaterials, 32, 681

AZoNano. 2012, Fundamentals of Contact Mode and Tapping Mode Atomic Force Microscopy, Tech. rep.

Badi, A. N., Kertesz, T. R., Gurgel, R. K., Shelton, C., & Normann, R. A. 2003, The Laryngscope, 113, 833

Bai, Q., & Wise, K. D. 2001, IEEE TRANSACTIONS ON BIOMEDICAL ENGINEERING, 48, 911

Bak, M. J., Salcman, M., & Schmidt, E. M. 1977, IEE Transations of Biomedical Engineering, 24, 121

Barres, B. A., Chun, Linda, L. Y., & Corey, D. P. 1989, 07970

Barrese, J. C., Rao, N., Paroo, K., et al. 2013, Journal of Neural Engineering, 10, 1

Basso, J. M. V., Yurchenko, I., Simon, M., Rizzo, D. J., & Staii, C. 2019, Physical Review E, 99, 1

Batlle, X., & Labarta, A. 2002, Journal of Physics D: Applied Physics, 35, R15

Bedell, H. W., Schaub, N. J., Capadona, J. R., & Ereifej, E. S. 2020, Acta Biomaterialia, 102, 205

Ben-johny, M., & Yue, D. T. 2014, The Journal of General Physiology, 143, 679

Bezuidenhout, D., Oosthuysen, A., Davies, N., et al. 2013, Journal of Biomedical Materials Research - Part A, 101 A, 1311

Bignami, A., & Dahl, D. 1976, Neuropathology and Applied Neurobiology, 2, 99

Bikbaev, A., Frischknecht, R., & Heine, M. 2015, Scientific Reports, 5, 1

Biran, R., Martin, D. C., & Tresco, P. a. 2005, Experimental Neurology, 195, 115

Blanche, T. J., Spacek, M. A., Hetke, J. F., et al. 2004, Journal of Neurophysiology, 93, 2987

Boroujerdi, A., Kee, H., Su, Y., et al. 2009, Pain, 139, 358

Brambilla, R., Persaud, T., Hu, X., et al. 2009, doi:10.4049/jimmunol.0802954

Brinen, J. S., & Melera, A. 1972, The Journal of Physical Chemistry, 76, 2525

Budday, S., Sommer, G., Birkl, C., et al. 2017, Acta Biomaterialia, 48, 319

Butt, H. J., Cappella, B., & Kappl, M. 2005, Surface Science Reports, 59, 1

Cabantous, S., Poudiougou, B., Bergon, A., et al. 2020, Mediators of Inflammation, 1

Cakir, B., Xiang, Y., Tanaka, Y., et al. 2019, Nature Methods, 16, 1169

Campbell, P. K., Huber, R., Horch, K. W., & A, N. R. 1991, IEE Transations of Biomedical Engineering, 38, 758

Catterall, W. A., Perez-reyes, E., Snutch, T. P., & Striessnig, J. 2019, Voltage-gated calcium channels (version 2019 . 4) in the IUPHAR / BPS Guide to Pharmacology Database, Tech. rep.

Chang, T. Y., Yadav, V. G., Leo, S. D., et al. 2007, 20, 11718

Cheli, V. T., González, D. A. S., Smith, J., et al. 2017, 64, 1396

Chen, H., Kim, G. S., Okami, N., Narasimhan, P., & Chan, P. H. 2011, Neurobiology of Disease, 42, 341

Chestek, C. A., Gilja, V., Nuyujukian, P., et al. 2011, Journal of Neural Engineering, 8, 1

Chung, J. E., Joo, H. R., Fan, J. L., et al. 2019, Neuron, 101, 21

Collection, I. D., Have, P.-s. H., New, R., & Cancer, B. 2018, 2017

Coronel, R., Lachgar, M., Bernabeu-zornoza, A., et al. 2019, Molecular Neurobiology, 56, 1248

Crosio, C., Valle, C., Casciati, A., Iaccarino, C., & Carrı, M. T. 2011, PLoS ONE, 6, 1

Csicsvari, J., Henze, D. A., Jamieson, B., et al. 2003, Journal of Neurophysiology, 90, 1314

Cui, X., & Martin, D. C. 2003, 89, 92

Dvoriantchikova, G., Barakat, D., Brambilla, R., et al. 2009, European Journal of Neuroscience, 30, 175

Dyson, K., Simmons, C. S., & Stewart, D. C. 2017, 1

Edell, D., Toi Van, V., McNeil, V., & Clark, L. 1992, IEE Transations of Biomedical Engineering, 39, 635

Eles, J. R., Vazquez, A. L., Snyder, N. R., et al. 2017, Biomaterials, 113, 279

Ereifej, E. S., Cheng, M. M. C., Mao, G., & VandeVord, P. J. 2013, Journal of Neuroscience Methods, 217, 17

Ereifej, E. S., Khan, S., Newaz, G., et al. 2011, Journal of Biomedical Materials Research - Part A, 99 A, 141

Ereifej, E. S., Rial, G. M., Hermann, J. K., Smith, C. S., & Meade, S. M. 2018a, Frontiers in Bioemgineering and Biotechnology, 6, 1

Ereifej, E. S., Smith, C. S., Meade, S. M., et al. 2018b, Advanced Functional Materials, 28, 1

Farrukh, A., Zhao, S., & del Campo, A. 2018, Frontiers in Materials, 5, 1

Ferreira, D. W., Guimaraes, R. M., Cecilio, N. T., et al. 2019, Pain, 160, 102

Fetz, E. 1969, Science, 163, 955

Flynn, J. M., & Melov, S. 2013, Free Radical Biology and Medicine, 62, 4

Fomchenko, E. I., & Holland, E. C. 2006, Clinical Cancer Research, 12, 5288

Foo, L. C., Allen, N. J., Bushong, E. A., et al. 2011, Neuron, 71, 799

Gardella, J. A., & Hercules, D. M. 1980, 226

Gilmour, A., Poole-warren, L., & Green, R. A. 2019, Frontiers in Neuroscience, 13, 1

Green, M., Bilstone, L., & Sinkus, R. 2008, NMR in Biomedicine, 21, 755

Green, R., & Abidian, M. R. 2015, Advanced materials (Deerfield Beach, Fla.), 27, 7620

Gregory, B., Thompson, C., Salatino, J., et al. 2021, IEEE Neural Engineering Research, 6

Guttenplan, K. A., Weigel, M. K., Prakash, P., et al. 2021, Nature, 1

Ham, O., Bae, Y., Kim, J., & Lee, M.-o. 2020, Biochemical and Biophysical Research Communications, 521, 84

Harnett, E. M., Alderman, J., & Wood, T. 2007, 55, 90

Hashioka, S., Klegeris, A., Qing, H., & Mcgeer, P. L. 2011, Neurobiology of Disease, 41, 299

He, W., McConnell, G. C., Schneider, T. M., & Bellamkonda, R. V. 2007, Advanced Materials, 19, 3529

Herrmann, J. E., Imura, T., Song, B., et al. 2008, Journal of Neuroscience, 28, 7231

Hess, A. E., Capadona, J. R., Shanmuganathan, K., et al. 2011, Journal of Micromechanics and Microengineering, 21, doi:10.1088/0960-1317/21/5/054009

Hetke, J. F., Williams, J CPellinen, D. S., Vetter, R. J., & Kipke, D. R. 2003, Proceedings of the 1st International IEEE EMBS, 181

Hochberg, L. R., Bacher, D., Jarosiewicz, B., et al. 2012, Nature, doi:10.1038/nature11076

Hochberg, L. R., Serruya, M. D., Friehs, G. M., et al. 2006, Nature, 442, 164

Hotchkiss, K. M., Ayad, N. B., Hyzy, S. L., Boyan, B. D., & Olivares-Navarrete, R. 2017, Clinical Oral Implants Research, 28, 414

Hotchkiss, K. M., Clark, N. M., & Olivares-Navarrete, R. 2018, Biomaterials, 182, 202

Hotchkiss, K. M., Reddy, G. B., Hyzy, S. L., et al. 2016, Acta Biomaterialia, 31, 425

Hotchkiss, K. M., Sowers, K. T., & Olivares-Navarrete, R. 2019, Dental Materials, 35, 176

Jin, X., Zhu, F., Mao, H., Shen, M., & Yang, K. H. 2013, Journal of Biomechanics, 46, 2795

Jr, R. R. R., Miller, J. A., & Reichert, W. M. 1993, 14

Kajihara, H., Tsutsumi, E., Kinoshita, A., Nakano, J., & Takagi, K. 2001, Brain Research, 909, 92

Kang, J., Jiang, L., Goldman, S. A., & Nedergaard, M. 1998, Nature, 1

Kanno, M., Suzuki, S., Fujiwara, T., et al. 2005, Journal of Neuroimmonolgy, 167, 72

Kato, Y., Saito, I., Hoshino, T., Suzuki, T., & Mabuchi, K. 2006, 2006 International Conference of the IEEE Engineering in Medicine and Biology Society, 660

Khan, S. P., Auner, G. G., & Newaz, G. M. 2005, Nanomedicine: Nanotechnology, Biology, and Medicine, 1, 125

Khurram, A., & Seymour, J. P. 2013, IEEE Engineering in Medicine and Biology, 3032

Kim, D. H., Viventi, J., Amsden, J. J., et al. 2010, Nature Materials, 9, 8

Kim, S.-p., Simeral, J. D., & Hochberg, L. R. 2008, Journal of neural engineering, 5, 455

Knaack, G. L., McHail, D. G., Borda, G., et al. 2016, Frontiers in Neuroscience, 10, 1

Kolarcik, C. L., Bourbeau, D., Azemi, E., et al. 2012, Acta Biomaterialia, 8, 3561

Kook, G., Lee, S. W., Lee, H. C., Cho, I. J., & Lee, H. J. 2016, Micromachines, 7, 1

Kovacs, G. T. A., Storment, C. W., & Rosen, J. M. 1992, IEEE Transactions on Biomedical Engineering, 30, 893

Kozai, T. D. Y., Catt, K., Li, X., et al. 2015a, Biomaterials, 37, 25

Kozai, T. D. Y., Jaquins-Gertsl, A. S., Vazquez, A. L., Michael, A. C., & Cui, X. T. 2015b, ACS Chemical Neuroscience, doi:10.1021/cn500256e

Lananna, B. V., Mckee, C. A., King, M. W., et al. 2020, Science translational medicine, 12, 1

Lee, H., Bellamkonda, R. V., Sun, W., & Levenston, M. E. 2005, Journal of Neural Engineering, 2, 81

Lei, H., Li, W., & Tan, X. 2014, Sensors & Actuators: A. Physical, 217, 1

Li, C., Nguyen, H. T., Zhuang, Y., et al. 2012a, Gene, 511, 143

—. 2012b, Gene, 511, 143

Li, K., Li, J., Zheng, J., & Qin, S. 2019, Aging and Disease, 10, 664

Li, Q., & Barres, B. A. 2017, Nature Publishing Group, 18, 225

Liddelow, S. A., & Barres, B. A. 2017, Immunity, 46, 957

Liddelow, S. A., Guttenplan, K. A., Clarke, L. E., et al. 2017, Nature, 541, 481

Lippert, S. A., Rang, E. M., & Grimm, M. J. 2004, 41, 681

Liu, T., Zhang, L., Joo, D., & Sun, S.-c. 2017, Nature, 2, 1

Ludwig, K. A., Joseph, D., Uram, J. D., et al. 2006, doi:10.1088/1741-2560/3/1/007

Luque, T., Kang, M. S., Schaffer, D. V., & Kumar, S. 2016, Royal Society open science, 3, 150702

Mammadov, B., Sever, M., Guler, M. O., & Tekinay, A. B. 2013, Biomaterials Science, 1, 1119

Matute-Blanch, C., Calvo-Barreiro, L., Carballo-Carbajal, I., et al. 2020, Scientific Reports, 10, 1

Mcconnell, G. C., Rees, H. D., Levey, A. I., et al. 2009, Journal of neural engineering, 6, 1

Mercanzini, A., Reddy, S. T., Velluto, D., et al. 2010, Journal of Controlled Release, 145, 196

Merienne, N., Schneider, A., Neri, C., et al. 2019, Cell Reports, 26, 2477

Metz, S., Bertsch, A., Bertrand, D., & Renaud, P. 2004a, Elsevier, 19, 1309

Metz, S., Bertsch, A., & Renaud, P. 2005, Journal of Microelectromechanical Systems, 14, 383

Metz, S., Trautmann, C., Bertsch, A., & Renaud, P. 2004b, Journal of Micromechanics and Microengineering, 14, 324

Michelson, N. J., Vazquez, A. L., Eles, J. R., et al. 2018, Journal of Neural Engineering, 15, 033001

Oakes, R. S., Polei, M. D., Skousen, J. L., & Tresco, P. A. 2018, Biomaterials, 154, 1

Okada, S., Nakamura, M., Katoh, H., et al. 2006, Nature Medicine, 12, 829

Pappalardo, L. W., Samad, O. A., Black, J. A., & Waxman, S. G. 2014, Glia, 62, 1162

Perea, G., & Araque, A. 2005, Journal of Neural Transmission, 112, 127

Pham, M. T., Pollock, K. M., Rose, M. D., et al. 2018, NeuroReport, 29, 588

Pijolat, M., & Hollinger, G. 1981, Surface Science, 105, 114

Pogoda, K., Chin, L., Georges, P. C., et al. 2014, New Journal of Physics, 16, doi:10.1088/1367-2630/16/7/075002

Polikov, V. S., Block, M. L., Fellous, J.-m., Hong, J.-s., & Reichert, W. M. 2006, Biomaterials, 27, 5368

Polikov, V. S., Tresco, P. a., & Reichert, W. M. 2005, Journal of Neuroscience Methods, 148, 1

Porter, J. T., & Mccarthy, K. D. 1995a

Porter, J. T., & Mccarthy, K. E. N. D. 1995b, 112, 101

Presumey, J., Bialas, A. R., & Carroll, M. C. 2017, Complement System in Neural Synapse Elimination in Development and Disease, 1st edn., Vol. 135 (Elsevier Inc.), 53–79, doi:10.1016/bs.ai.2017.06.004

Quail, D. F., & Joyce, J. A. 2017, Cancer Cell, 31, 326

Robert, S. M., Buckingham, S. C., Campbell, S. L., et al. 2015, Science Translational Medicine, 7, doi:10.1126/scitranslmed.aaa8103.SLC7A11

Roman, G. C., Mancera-Paez, O., & Bernal, C. 2019, International Journal of Molecular Science, 20, 1

Roshanbin, S., Lindberg, F. A., Lekholm, E., et al. 2016, BMC Neuroscience, 17, 1

Rousche, P. J., & Normann, R. A. 1999, 7, 56

Rutkowska, A., Preuss, I., Gessier, F., Sailer, A. W., & Dev, K. K. 2015, Glia, 63, 341

Salatino, J. W., Kale, A. P., & Purcell, E. K. 2019

Salatino, J. W., Ludwig, K. A., Kozai, T. D., & Purcell, E. K. 2017, Nature Biomedical Engineering, 1, 862

Salatino, J. W., Ludwig, K. A., Kozai, T. D. Y., & Purcell, E. K. 2018, Nature Biomedical Engineering, 2, 52

Schmidt, E., Macintosh, S., & Bak, M. 1988, Medical & Biological Engineering & Computing, 26, 96

Seymour, J. P., & Kipke, D. R. 2007, Biomaterials, 28, 3594

Seymour, J. P., Langhals, N. B., Anderson, D. J., & Kipke, D. R. 2011, 441

Shearer, M. C., & Fawcett, J. W. 2001, Cell Tissue, 267

Shen, H.-b., Long, D.-h., Zhu, L.-z., et al. 2006, Biophysical Chemistry, 122, 1

Shigetomi, E., Kracun, S., Sofroniew, M. V., & Khakh, B. S. 2010, Nature Neuroscience, 14, 759

Simeral, J. D. 2011, doi:10.1088/1741-2560/8/2/025027

Stephenson, D., Rash, K., Smalstig, B., et al. 1999, Glia, 128, 110

Stieglitz, T. 2001, Elsevier, 90, 203

Stieglitz, T., Beutel, H., & Meyer, J.-U. 1997, Elsevier, 60, 240

Stiller, A. M., Black, B. J., Kung, C., et al. 2018, Micromachines, 9, 1

Strumwasser, F. 1958, Science, 127, 469

Subbaroyan, J., Martin, D. C., & Kipke, D. R. 2005, Journal of Neural Engineering, 2, 103

Suner, S., Fellows, M. R., Vargas-irwin, C., Nakata, G. K., & Donoghue, J. P. 2005, IEEE Transactions on Neural Systems and Rehabilitation Engineering, 13, 524

Szarowski, D. H., Andersen, M. D., Retterer, S., Spence, A. J., & Isaacson, M. 2003, 983, 23

TAMURA, A., HAYASHI, S., WATANABE, I., NAGAYAMA, K., & MATSUMOTO, T. 2007, Journal of Biomechanical Science and Engineering, 2, 115

Thompson, C., Riggins, T., Patel, P., et al. 2019, Journal of Neural Engineering

Thompson, C. H., Riggins, T. A. E., Patel, P. R., et al. 2020, Journal of Neural Engineering, 17, 1

Thompson, C. H., Saxena, A., Heelan, N., Salatino, J., & Purcell, E. K. 2021, Journal of Neural Engineering, 18, 1

Tien, L. W., Wu, F., Tang-Schomer, M. D., et al. 2013, Advanced Functional Materials, 23, 3185

Vappou, J., Breton, E., Choquet, P., et al. 2007, Magnetic Resonance Materials in Physics, Biology and Medicine, 20, 273

Wade, A., Robinson, A. E., Engler, J. R., et al. 2013, FEBS Journal, 280, 2399

Wadhwa, R., Lagenaur, C. F., & Cui, X. T. 2006, Journal of Controlled Release, 110, 531

Ware, T., Simon, D., Liu, C., et al. 2013, 1

Wei, L., Zhang, J., Zhang, B., et al. 2020, Brain Research, 1726, 146423

Weisenberg, B. A., & Mooradian, D. L. 2001, doi:10.1002/jbm.10076

Wilson, C. L., Hayward, L., & Kidambi, S. 2016, 34447

Wise, K., Angell, J., & Starr, A. 1970, IEEE Trans Biomedical Engineering, 17, 238

Wise, K. D., Anderson, D. J., Hetke, J. F., Kipke, D. R., & Najafi, K. 2004, Proceedings of the IEEE, 92, 76

Wise, K. D., & Angell, J. B. 1975, IEE Transations of Biomedical Engineering, 22, 212

Wörsdörfer, P., Dalda, N., Kern, A., et al. 2019, Scientific Reports, 9, 1

Yang, K.-H., & Narayan, R. J. 2019, Current Opinion in Biomedical Engineering, 10, 60

Zamanian, J. L., Xu, L., Foo, L. C., et al. 2012, Journal of Neuroscience, 32, 6391

Zhong, Y., & Bellamkonda, R. V. 2007, Brain Research, 1148, 15

Zhu, M., Allard, J. S., Zhang, Y., et al. 2015, Journal of Neuropathology and Experimental Neurology, 73, 362